Nucleic Acids Research, 2026, **54**, gkag181
https://doi.org/10.1093/nar/gkag181
Molecular and Structural Biology

Mechanism of interaction between the transactivation domain of N-myc and the DNA-binding surface of TFIIIC5

Eoin Leen [1,2,*], Sharon Yeoh [1,2], Eka Sahak [1], Ellie Mitchell [1], Gemma Wildsmith [1,2], Matthew Batchelor [1,2], Antonio N. Calabrese [1,2], Gabriele Büchel [3,4,5], Richard Bayliss [1,2,*]

[1]School of Molecular and Cellular Biology, Faculty of Biological Sciences, University of Leeds, Leeds LS2 9JT, United Kingdom
[2]Astbury Centre for Structural Molecular Biology, University of Leeds, Leeds LS2 9JT, United Kingdom
[3]Theodor Boveri Institute, Department of Biochemistry and Molecular Biology, Biocenter, University of Würzburg, 97074 Würzburg, Germany
[4]Comprehensive Cancer Center Mainfranken, 97080 Würzburg, Germany
[5]Mildred Scheel Early Career Center, University Hospital Würzburg, 97080 Würzburg, Germany

*To whom correspondence should be addressed. Email: e.leen@leeds.ac.uk
Correspondence may also be addressed to Richard Bayliss. Email: r.w.bayliss@leeds.ac.uk

Abstract

N-myc is a transcription factor, a powerful driver of cellular growth and an important oncoprotein. N-myc interacts with many factors, including the RNA Polymerase III assembly factor, TFIIIC, a six-subunit complex that is essential for the transcription of small, structured RNA. TFIIIC and N-myc mutually restrict each other's chromatin association, and their complex contributes to quality control in mRNA transcription. We previously demonstrated that the intrinsically disordered transactivation domain of N-myc interacts directly with a sub-complex of TFIIIC, τA. Structural studies by others show that DNA binding of τA is largely mediated by TFIIIC3, leaving open the role of the DNA-binding domain of TFIIIC5. Here, we demonstrate that this domain is a binding site for two regions in the transactivation domain of N-myc, through an integrated approach combining NMR spectroscopy, hydrogen–deuterium exchange mass spectrometry, and interaction assays (pull-downs, ITC, fluorescence polarization, and co-immunoprecipitation). AlphaFold modelling predicts with high-confidence a binding mode for the higher affinity N-myc motif that overlaps with the predicted intramolecular binding site of the C-terminal acidic plug of TFIIIC5, removal of which enhances the binding of N-myc. This model elucidates how the N-myc:TFIIIC5 interaction competes with DNA and other interactions, providing a basis for their mutual regulation.

Graphical abstract

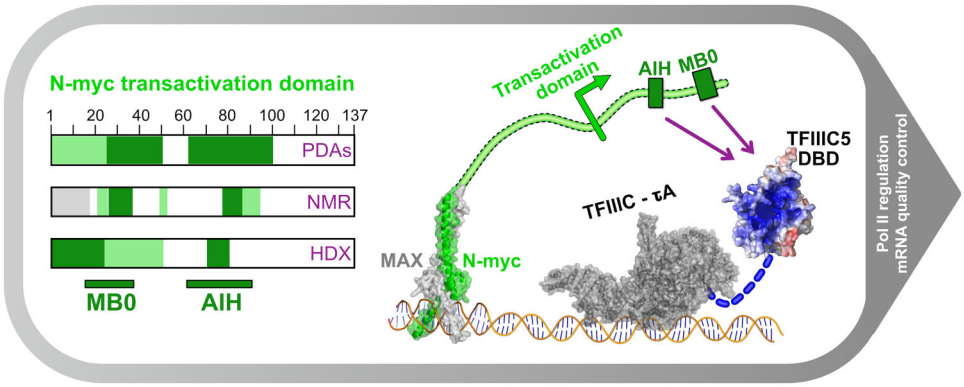

Introduction

The myc family of transcription factors (c-myc, N-myc, and L-myc) is a homologous group of basic Helix–Loop–Helix transcription factors. They are largely intrinsically disordered; however, their C-terminus is known to form a basic Helix–Loop–Helix leucine zipper domain with its constitutive binding partner, MAX [1]. This complex binds preferentially to six base-pair DNA sequences known as E-boxes [2, 3].

Myc family members have physiological roles in development and tissue homeostasis, and they are very important drivers of oncogenesis [4]. Of 11 000 samples covering 33 cancer types, that were tested from the Pan Cancer Genome Atlas, 28% were found to be copy number amplified for a myc family member [5]. Myc is thought to be a non-linear amplifier of transcription, acting to amplify existing transcriptional programs [6–8]. Myc is an activator of all three metazoan DNA-dependent RNA polymerases, Pol I (rRNA, ribosomal RNA),

Received: October 22, 2024. **Revised:** February 7, 2026. **Accepted:** February 11, 2026

Pol II (mRNA, messenger RNA), and Pol III (tRNA, transfer RNA, and other small structured RNA species) [9–12].

The mechanisms by which myc activates transcription are still incompletely defined. However, myc has many binding partners in cells including proteins involved in chromatin structure and transcriptional regulation [13, 14]. Both c-myc and N-myc increase the phosphorylation of serine 2 in the C-terminal heptad repeat of Pol II, which facilitates the release of the polymerase from a pause in a promoter proximal region into the gene body [14, 15]. More recently, c-myc has been shown to increase the duration of transcriptional bursts and increase the dwell time of known transcriptional activator proteins at promoters [16]. Additionally, at high concentrations, N-myc forms phase separated foci with other molecules suggestive of active transcription such as the mediator complex and nascent RNA [17]. While regulation of transcription by myc proteins is complex and multi-faceted, it is likely to be driven by protein–protein interactions between myc proteins and regulators of transcription such as general transcription factors.

N-myc is an important driver of neuroendocrine cancers such as neuroblastoma, a malignancy of early-stage sympathetic neurons which occurs in children [18]. N-myc was discovered in a neuroblastoma cell line, and its genomic amplification is a prognostic indicator of neuroblastoma disease progression [19–21]. N-myc can functionally replace c-myc in murine development, suggesting that these proteins are redundant, to a large extent [22]. These conserved functions are likely to be mediated primarily through conserved sequences known as myc boxes. The first three myc boxes (MB0, MBI, and MBII) are contained within the transactivation domain of the protein which comprises the N-terminal ∼150 residues of myc family members. This region is essential for both transcriptional transactivation and oncogenic functions of the protein [13, 23].

The TFIIIC complex is a general transcription factor which has been repeatedly demonstrated to interact with both N-myc and c-myc in cells using both affinity capture mass spectrometry and biotin labelling mass spectrometry approaches [13, 14, 24–27]. TFIIIC is a six-subunit complex which has a well-defined role in the recruitment of Pol III to the promoters of small, structured RNA encoding genes such as tDNA genes. TFIIIC binds to conserved sequences, known as A and B boxes, and recruits another transcription factor complex, TFIIIB. TFIIIB in turn recruits Pol III. TFIIIC is composed of two sub-complexes, τA and τB, which bind to A-box and B-box DNA sequences, respectively. The two domains are linked flexibly to account for the variable distance between A and B-box sequences in promoter regions [28].

Until recently, human τA was thought to consist of 3 subunits: TFIIIC3, TFIIIC5, and TFIIIC6. τB was thought to be composed of TFIIIC1, TFIIIC2, and TFIIIC4, with TFIIIC1 acting as the flexible linker between the sub-complexes. However, recent cryo-EM structures of human TFIIIC bound to promoter DNA, and the yeast TFIIIA–TFIIIC–TFIIIB complex bound to promoter DNA, both showed that TFIIIC1 contributes domains to both subcomplexes and as such should be considered a constitutive member of both τA and τB [29, 30]. Other constitutive members of the τA sub-complex include TFIIIC3, a ∼100 kDa protein with two large and nearly contiguous tetratricopeptide repeat (TPR) domains. These TPR domains act as a hub for protein-protein interactions, for example in recruitment of the TFIIIB complex [31, 32]. TFIIIC3 has additionally been shown to extensively bind promoter DNA [30, 33].

TFIIIC5 contains two domains. There is an N-terminal dimerization domain which forms a heterodimerization β-barrel domain with TFIIIC6 [29, 34, 35]. TFIIIC6 consists only of this domain, unlike the equivalent protein in yeast which additionally contains a histidine phosphatase domain. The C-terminal domain of TFIIIC5 is a DNA-binding domain (DBD), which connects via an acidic low complexity sequence to a C-terminal helix, termed the acidic plug, which packs back into the DNA-binding surface [34, 35].

N-myc acts in concert with TFIIIC, primarily on Pol II (mRNA) transcription rather than Pol III transcription [14, 36]. The complex plays a role in transcript quality control facilitating the recruitment of BRCA1 and the nuclear exosome complex to stalled transcripts [36]. How N-myc interacts with the TFIIIC complex is a work in progress. We have previously shown that the transactivation domain of N-myc (1–137) interacts directly with the τA sub-complex of TFIIIC [36]. We have additionally shown that TFIIIC competes with Aurora-A kinase for N-myc binding. This was demonstrated *in vitro* using pull-downs with recombinant bait proteins and HeLa lysate, as well as through proximity ligation assays in cells [14, 36]. Here, we demonstrate that the DBD of TFIIIC5 is a major interaction site for N-myc, determine the crystal structure of the human DBD, and elucidate the molecular basis of the interaction using an integrated biochemical, biophysical, and computational approach. Finally, we have validated our findings using immunoprecipitation experiments in a neuroblastoma cell line expressing WT or a variant N-myc protein. The model defines the TFIIIC5 DBD as a regulatory hub for N-myc association and supports a generalized mechanism in which the Myc MB0 region competes with DNA for transcription factor binding.

Materials and methods

Plasmids

Protein sequences including vectors and tags used in the study are described in Supplementary Table S1. pCDFDuet-1, pETM6T1, pGEX-6P-1, and pET30TEV were the vectors used for *Escherichia coli* expression. pGEX-6P-1 and pCDFDuet-1 are both commercially available vectors from Cytiva and Merck, respectively. pETM6T1 is a modified version of pET44b producing a TEV Nia cleavable 6xHis-NusA fusion protein [37]. pET30TEV is a modified pET30a plasmid with a TEV Nia site added after the NspV replacing a large part of the S-tag and all of the enterokinase cleavage site. pCDFDuet-1 monomeric ultra-stable GFP (muGFP) fusion clones were made in a two-step process. First, an *E. coli* codon optimized DNA sequence was synthesized by GeneArt, this coded for an N-terminal 6xHis tag followed by a short linker and an muGFP sequence. This was followed by another short linker and then a TEV Nia site. The TEV site was followed immediately by an in-frame BamHI restriction site which was followed by a 51 base pair sequence and an EcoRI site. The N-terminal start codon was within an NcoI restriction site. NcoI and EcoRI sites were used to ligate the sequence into pCDFDuet-1 (Novagen). *E. coli* codon optimized sequences were ordered from Twist Biosciences and GeneArt which code for TFIIIC3 TPR1 (residues 143–578; Uniprot: Q9Y5Q9), TFIIIC3 TPR2 (residues 578–886; Uniprot: Q9Y5Q9), and

TFIIIC5 DBD (residues 212–519; Uniprot: Q9Y5Q8). These were designed to have a 5′ BamHI site and a 3′ EcoRI site for cloning into the pCDFDuet-1-muGFP vector described above. In the case of the TFIIIC5|6 dimerization domain a DNA cassette was ordered from Twist biosciences which enabled co-expression of these two proteins in the pCDFDuet-1-muGFP vector. The sequence contained a 5′ BamHI site followed by an *E. coli* optimized TFIIIC5 dimerization domain sequence (residues 1–130; Uniprot: Q9Y5Q8) this was followed by an EcoRI site, and then the sequence of pCDFDuet-1 until the NdeI site in the second Multiple cloning site. The ATG sequence of the NdeI site was the start codon in an *E. coli* codon optimized TFIIIC6 DNA sequence (encoding for residues 1–213; Uniprot: Q969F1). This coding sequence was followed by a 3′ XhoI site. The BamHI and XhoI sites were used to clone this entire cassette into the pCDFDuet-1-muGFP vector.

A TFIIIC5 DBD protein sequence was designed to optimize expression of the domain. This design, referred to as TFIIIC5 DBD ΔΔ, begins at 208 and truncates a large loop within the domain, removing residues 345–366 inclusive. The C-terminus of the protein was also truncated to 470 (from 519), removing an intrinsically disordered region (IDR), including a low complexity acidic region, and a C-terminal helical region known as the acidic plug. A DNA sequence encoding this protein was codon optimized for *E. coli* and synthesized by GeneArt. Flanking 5′ BamHI site and 3′ EcoRI and XhoI sites were used for cloning. BamHI and EcoRI were used for cloning into pCDFDuet-1-muGFP and pGEX-6P-1. BamHI and XhoI sites were used for cloning into pET30TEV. Similarly, a DNA sequence was produced which encoded a TFIIIC5 DBD ΔΔ variant that built back the acidic plug region of the protein. This is referred to as ΔΔ+AP. This protein sequence is the same up to residue 470. Instead of truncating at this point it continues to the authentic C-terminus at 519, with deletion of the low complexity acidic sequence from 487 to 500 inclusive. This construct was synthesized by GeneArt to have the same DNA sequence as TFIIIC5 ΔΔ for the regions with identical protein sequence. It also contained the same flanking sequences for cloning into pET30TEV. DNA sequences encoding N-myc were previously cloned from cDNA. N-myc (UniProt: P04198) sequences were expressed from the following plasmids: pET30TEV N-myc 1–137, pETM6T1 N-myc 1–137, pETM6T1 GB1-N-myc 18–72 C27S, pETM6T1 GB1-N-myc 18–59 C27S, and pETM6T1 N-myc 64–137. The GB1 fusion tag construct has been described elsewhere [38].

Full-length WT and F28A-Y29A N-myc proteins were used in immunoprecipitation assays. GeneArt Strings (Thermo Fisher scientific) encoding FL N-myc with an N-terminal Ha tag (MYPYDVPDYAGG) were used to clone N-myc DNA into pRRL. AgeI and SpeI restriction enzyme sites were the 5 and 3 sites respectively. The DNA sequences were codon optimized for expression in human cells, and are identical except for the F28A-Y29A mutations.

Protein expression

Proteins were expressed in *E. coli* BL21(DE3)-RIL cells. 35 μg/ml chloramphenicol was used to select for the RIL plasmid. 50 μg/ml of kanamycin and spectinomycin was used to select for pET and pCDF vectors, respectively. 100 μg/ml ampicillin was used to select for pGEX-6P-1. 10 ml of an overnight culture was added to each litre of LB media. The cells were grown at ∼200 RPM and 37°C until mid-log phase (OD_{600} ∼0.6) and then shifted to room temperature for approximately 30 min. Expression was induced by addition of 0.6 mM IPTG. The cells were grown overnight (16–19 h) at ∼200 RPM and 20°C prior to harvesting at 6000 × *g* for 15 min. Pellets were stored at −80°C prior to processing. Expression of NMR labelled protein was performed exactly as described elsewhere [38].

Protein purification

All steps were performed on ice or at 4°C. A detailed list of buffers at each stage of purification, and for each protein purified, are outlined in Supplementary Table S2. *E. coli* pellets were resuspended in initial purification buffer (IPB) (Supplementary Table S2) that had been spiked with ∼10 mg of lysozyme (Sigma–Aldrich), 750 U Benzonase nuclease (Merek), and 1 tablet of Roche cOmplete EDTA-free protease inhibitor cocktail, for each 30 ml of lysis buffer. Typically, 15 ml of lysis buffer was used per litre of LB media used in expression. Initially pellets were disrupted by pipetting and then by sonication. Lysate was clarified by centrifugation at 40 000 × *g* for 20 min and applied to buffer equilibrated His-select Cobalt affinity gel (Sigma–Aldrich). Eluted protein was collected and dialysed overnight against 4 l of dialysis buffer (Supplementary Table S2) using either 3.5 kDa or 10 kDa molecular weight cut off SnakeSkin dialysis tubing (Pierce) as appropriate. For all His-tagged proteins except the 6xHis-muGFP tagged proteins, TEV Nia was used to remove the His-tag during dialysis. 0.45 or 0.9 mg of His-tagged TEV Nia was added to the protein, depending on the yield, and incubated overnight during dialysis. Lysate containing GST-tagged TFIIIC5 DBD ΔΔ protein was loaded onto gluthatione-4B resin, washed with IPB buffer, and eluted by addition and overnight incubation with 1 mg of PreScission protease. Post-dialysis His-tagged TEV Nia-processed proteins were further purified by cobalt resin subtraction, using supplemented with low concentrations of imidazole to elute the untagged proteins. Untagged N-myc protein was typically in the 0, 5, and 10 mM imidazole fractions whereas the untagged TFIIIC5 DBD ΔΔ proteins required up to 30 mM imidazole. Two proteins used in the study were purified by ion-exchange chromatography prior to size exclusion chromatography (SEC). The first was 6xHis-muGFP tagged TFIIIC5 DBD, because the initial affinity purified protein contained a contaminant of similar molecular weight. The post-dialysis protein was loaded into a 5 ml Q fast-flown column. The flow was collected and a linear gradient of low NaCl (25 mM Tris pH 8, 150 mM NaCl, and 2 mM β-mercaptoethanol) to high NaCl buffer (25 mM Tris pH 8, 500 mM NaCl, and 2 mM β-mercaptoethanol) applied over 60 ml. The contaminant and 6xHis-muGFP tagged TFIIIC5 DBD eluted at different conductivity values, which were approximately 18–26 and 27–35 mS/cm, respectively. The second protein for which ion-exchange was performed was N-myc 1–137 expressed with a 6xHis-NusA tag. This was performed very similarly to that previously outlined except using the following buffers: Low salt: 25 mM Tris pH 7.4, 137 mM NaCl, 2.7 mM KCl, 2 mM β-mercaptoethanol; High salt: 25 mM Tris pH 7.4, 537 mM NaCl, 2.7 mM KCl, 2 mM β-mercaptoethanol. In this case, N-myc eluted over a wide range of fractions. These were pooled prior to cobalt resin subtraction. SEC was performed as a final polishing step on all purified proteins using a HiLoad Superdex 75 16/60 column

connected to an ÄKTA Prime FPLC. Pure fractions were pooled and concentrated in centrifugal concentrators of appropriate molecular weight cut off. Protein concentrations were determined using absorbance at 280 nm and extinction coefficients calculated using Protparam. Proteins were aliquoted into 30–50 μl volumes and snap frozen in liquid nitrogen and stored at −80°C. TFIIIC5 which had been purified with a GST-tag exhibited DNA contamination, and so was treated with 2500 U of Benzonase nuclease with 2 mM $MgCl_2$ and 1 mM $MnCl_2$ for 36 h at 4°C prior to SEC. N-myc 1–137 with a 6xHis-tag was purified from inclusion bodies, a process that has been described previously [36].

His-tagged based pull-down assays

37.5 μl of His-select cobalt affinity resin (Sigma–Aldrich) equilibrated with mix buffer (25 mM Tris pH 8, 100 mM NaCl, 2 mM β-mercaptoethanol, and 0.064% Tween-20) was used for each pull-down. 6xHis-muGFP tagged TFIIIC domains (TFIIIC3 TPR1; TFIIIC5 DBD; TFIIIC5 DBD ΔΔ, TFIIIC5|6 dimer) were used as bait. Untagged N-myc 1–137 was used as prey. Bait and prey proteins were combined with mix buffer to a final volume, excluding resin, of 425 μl. Final bait and prey concentrations were 10 and 15 μM, respectively. Bait protein, bait protein buffer, prey protein and mix buffer were mixed so that the final concentration of each component was identical across all pull-downs. The mixture was rotated slowly at 4°C for 60 min. 10 μl of mix was taken for analysis. The slurry was centrifuged at 5000 × *g* for 30 s at 4°C. The supernatant was removed, and the resin washed with 425 μl of mix buffer this was centrifuged at 5000 × *g* for 30 s at 4°C. The supernatant was removed, and the resin washed twice more. Protein was eluted by addition of 60 μl of mix buffer supplemented with 250 mM imidazole. The resin was centrifuged at 16 100 × *g* for 60 s and the supernatant taken as the elution fraction. 7 μl (including 3.5 μl of 2× SDS loading buffer) of both mix and elution fractions were run on SDS–PAGE gels for Coomassie stained gels. 2 μl were run for western blot analysis. For western blots transfer was performed to 0.2 μm nitrocellulose. Blocking was performed with PBST (PBS spiked with 0.1% Tween-20) spiked with 5% w/v dried low-fat milk. The blot was blocked by slow rotation at room temperature over a period of 30 min with three changes in blocking buffer. Anti-N-myc antibody (Santa Cruz - sc-53993) was diluted for 1/1000 in blocking buffer. This primary antibody was incubated with the blot for 60 min by slow rotation at room temperature. The blot was washed with PBST by slow rotation at room temperature with three changes of PBST over 30 min. The secondary antibody was a HRP conjugated anti-mouse antibody (Cytiva - NA931). This was diluted 1/2000 in blocking buffer and applied to the blot by slow rotation at room temperature for 60 min. The blot was then washed twice for 10 min with PBST. ECL substrate was applied for detection and blots were imaged using an iBright 1500 imager (Invitrogen).

NMR titrations

^{1}H-^{15}N HSQC experiments were used to monitor N-myc chemical shifts upon titration with TFIIIC5 DBD. These were performed using an Oxford Instruments 750 MHz magnet equipped with a Bruker TCI cryoprobe and AVANCE III HD console. The temperature was 283 K. The pulse sequence was hsqcetfpf3gpsi performed with standard parameters. 2048 (complex) points were recorded in the direct ^{1}H dimension, 488 (complex) points were recorded in the indirect ^{15}N dimension. Spectral widths were 8971.292 Hz for ^{1}H (∼12 ppm) and 1968.504 Hz for ^{15}N (∼26 ppm). Acquisition times were 0.114 s (F2, ^{1}H) and 0.124 s (F1, ^{15}N) with a relaxation delay of 1.0 s. Initially, two different ^{15}N labelled N-myc proteins were used: an N-terminal fusion of GB1 with N-myc 18–72 and tagless N-myc 64–137. N-myc 18–72 has a conservative substitution; C27S. Unlabelled TFIIIC5 DBD ΔΔ was used as the titrant. Proteins were all in a buffer containing 25 mM HEPES pH 6.9, 150 mM NaCl, and 2 mM β-mercaptoethanol. 5% D_2O was added for signal locking. The initial concentrations of proteins were as follows: GB1-N-myc 18–72 – 224 μM, N-myc 64–137 – 72 μM, and TFIIIC5 DBD ΔΔ – 567 μM. The following titration series of ΔΔ into labelled N-myc proteins were performed. For GB1-N-myc 18–72: reference (4 transients), 0.1 mole equivalents (4 transients), 0.3 mole equivalents (10 transients), 0.45 mole equivalents (12 transients), and 0.9 mole equivalents (64 transients). For N-myc 64–137: reference (8 transients), 0.1 mole equivalents (8 transients), 0.2 mole equivalents (8 transients), 0.35 mole equivalents (8 transients), 0.45 mole equivalents (16 transients), 0.8 mole equivalents (24 transients), and 1.5 mole equivalents (48 transients). Data were processed using NMRPipe and analysed used CcpNmr Analysis version 2.5 [39, 40]. Peak lists were imported from previous N-myc 1–137 assignments (BMRB entries: 52 047, 52 066, and 52 067). Overlapping peaks were excluded from the analysis. For each spectra peak maxima were automatically determined, and peak heights recorded. For intensity analysis the peak heights of the 0.1 mole equivalent peaks were divided by their reference equivalents. Error estimates (ΔR) for intensity ratios (R) were determined using the 'showApod' command of NMRpipe. This was used to determine the noise in each spectrum (Δx, Δy). Errors were propagated using $(\Delta R/R)^2 = (\Delta x/x)^2 + (\Delta y/y)^2$, where x and y are peak intensities in each spectrum. The ^{1}H-^{15}N TROSY experiments, used to follow the titration of TFIIIC5 DBD ΔΔ into ^{15}N labelled GB1-N-myc 18–59 C27S, were performed similarly to the experiments outlined previously with the following changes. The experiment was performed at 285 K. The pulse sequence used was a ^{1}H–^{15}N-Best TROSY with the following acquisition parameters. 2048 (complex) points were recorded in the direct ^{1}H dimension, 488 (complex) points were recorded in the indirect ^{15}N dimension. The spectral widths were 12 and 26 ppm in ^{1}H and ^{15}N, respectively. The D1 relaxation delay was 0.35 s. The initial protein concentrations were GB1-N-myc 18–59 at 50 μM and TFIIIC5 DBD ΔΔ at 927 μM. The titration series included: reference spectrum (16 transients), 0.1 mole equivalents (16 transients), 0.2 mole equivalents (32 transients), and 1.0 mole equivalents (144 transients).

NeutrAvidin based pull-down assays

N-terminally biotinylated N-myc peptides were used as bait in pull-downs with untagged TFIIIC5 DBD ΔΔ as prey. The peptides were synthesized by GenScript at ≥ 95% purity. They were dissolved to high concentrations (≥1 mM) using DMSO. The N-myc peptides included the following 1–25, 26–50, 51–75, 62–89, 76–100, 101–125, and 117–141. Assay buffer (25 mM Tris pH 7.4, 137 mM NaCl, 2.7 mM KCl, 1 mM β-mercaptoethanol, and 0.03% Tween-20), was used to dilute the biotinylated N-myc peptides to 20 μM. Seven aliquots

containing 40 μl of bed-volume of NeutrAvidin agarose resin (Thermo Fisher Scientific), was equilibrated by a single wash with pull-down buffer, prior to the addition of 450 μL of each respective peptide at 20 μM concentration. One peptide was used for each resin aliquot. After incubation of this slurry for 1 h, the resin was pelleted and the supernatant removed. The beads were then washed three times by the addition of 500 μl of pull-down buffer, centrifugation to pellet the resin, followed by removal of the supernatant. 460 μl of 12.5 μM TFIIIC5 DBD ΔΔ prey protein was then added to the resin and left to incubate by slow rotation for 2 h. Following this incubation period, 10 μl of mix was taken for analysis. The slurry mixture was washed three times and the proteins eluted from the beads by addition of 50 μl of 2× SDS loading buffer. SDS–PAGE was used to analyse both mix and bound fractions. Gels were stained with Coomassie stain. ImageJ was used to quantify the TFIIIC5 DBD ΔΔ bands in the bound fractions.

Isothermal titration calorimetry

Untagged TFIIIC5 DBD ΔΔ (pET30TEV expressed) and untagged N-myc 1–137 (pETM6T1 expressed), were both dialysed, overnight at 4°C, against 1 l of buffer (25 mM Tris pH 7.4, 137 mM NaCl, 2.7 mM KCl, and 2 mM β-mercaptoethanol) using Pur-A-Lyzer Midi 3.5 kDa molecular weight cut off dialysers (Sigma–Aldrich). ITC was performed using a MicroCal ITC200 (Malvern). A final concentration of 180.4 μM TFIIIC5 DBD ΔΔ was used in the syringe. A final concentration of 15.2 μM N-myc 1–137 was used in the cell. A total of 20 injections were performed into the cell, the first of 0.5 μl, the remaining 19 of 2 μl. 150 s was used as equilibration time between injections. The experiment was performed at 10°C. The stirring speed was 750 RPM. Data were analysed using the Origin software supplied with the instrument. A 1:1 binding model was used to fit the data.

Fluorescence polarization assays

N-myc peptides were used as tracers in fluorescence polarization (FP) assays with untagged TFIIIC5 DBD proteins (ΔΔ and ΔΔ+AP) (all pET30TEV expressed). N-terminally 5-carboxyfluorescein (FAM)-labelled N-myc peptides were synthesized by Peptide Synthetics to a purity of >95%. These were dissolved to a stock concentration of 10 mM using DMSO (dimethyl sulfoxide). Protein was diluted into assay buffer (25 mM Tris pH 7.4, 137 mM NaCl, 2.7 ml KCl, 1 mM β-mercaptoethanol, and 0.03% Tween-20) to a working stock (typically 62.5 μM). A two-fold dilution series was performed on this working stock, using assay buffer, to create the protein concentration gradient for the assay. Ten to fourteen two-fold dilutions were performed using the working stock, depending on the assay. 40 μl of the protein series was pipetted into black flat-bottomed 96-well assay plates. 10 μl working stock of peptide was then pipetted into the wells. FP was measured using a Victor X5 plate reader (Perkin Elmer). Excitation and emission wavelengths were 480 and 535 nm, respectively. Titrations were performed with three technical replicates, which were repeated in independent experiments using the same stocks of reagents between two and four times, three times in most cases. Data were fitted for each individual technical replicate using a one site total binding model ($Y = B_{max}*X/(K_D + X) + NS*X + Background$) in GraphPad Prism (Version 9). Results are reported as mean K_D ± one standard deviation.

X-ray crystallography

N-terminally acetylated N-myc 73–89 peptide was bought from Peptide Synthetics (Southampton, UK). Peptide was dissolved in a buffer (25 mM HEPES pH 7.5, 100 mM NaCl, and 1 mM TCEP). Titration of the pH up to approximately pH 7.0 was required for full solubilization. 1.07 mM peptide was incubated with 10 mg/ml (358 μM) untagged TFIIIC5 DBD ΔΔ (pET30TEV expressed) for 45 min on ice. Precipitation was removed from the sample by centrifugation at 13 100 × *g* for 1 min. Sitting drop vapor diffusion crystallization trials were set up using a Mosquito nanolitre pipetting system (TTP Labtech). 100 nl reservoir and 100 nl protein solution were mixed in two-well MRC crystallization plates. The drops were allowed to equilibrate against 85 μl of reservoir solution. As the crystals grew in a low molecular weight PEG condition (0.1 M phosphate/citrate pH 4.2 and 40% PEG 300), they were flash frozen in liquid N_2 directly from the small-scale setup. Data were collected at Diamond Light Source I04 (wavelength 0.9537 Å) beamline using a Eiger2 XE 16M detector. 3600 images were collected at 0.1° oscillation. Initial data processing was performed using the DIALS XIA2 automatic processing pipeline. The structure was phased by molecular replacement using the PhaserMR GUI within PHENIX. An AlphaFold2 model of the TFIIIC5 DBD ΔΔ was used as the molecular replacement solution following modification of the model in the process predicted model GUI in PHENIX. A combination of PHENIX AutoBuild, followed by iterative rounds of manual adjustments in Coot and PHENIX refine was used to finalize the structure.

Hydrogen–deuterium exchange

Hydrogen–deuterium exchange (HDX) experiments were conducted using an automated robot (LEAP Technologies) that was coupled to an Acquity M-Class LC with HDX manager (Waters). 447 μM TFIIIC5 DBD ΔΔ (pET30TEV expressed) and 361 μM N-myc 1–137 (pETM6T1 expressed) were diluted to 10 and 50 μM, respectively, in buffer made up with H_2O (8.09 mM Na_2HPO_4, 1.47 mM KH_2PO_4, 137 mM NaCl, and 2.7 mM KCl, pH 7.4). Experiments were performed with both components alone, or with both proteins mixed. Buffers were exactly matched in the mixed experiment. To initiate the HDX reaction, 95 μl of buffer made up with D_2O (8.09 mM Na_2HPO_4, 1.47 mM KH_2PO_4, 137 mM NaCl, and 2.7 mM KCl, pD 7.4) was transferred to 5 μl of protein-containing solution, and the mixture was subsequently incubated at 4°C for 0.5, 5, or 30 min. Three replicate measurements were performed for each time point and condition studied. 50 μl of quench buffer (8.9 mM Na_2HPO_4, 1.5 mM KH_2PO_4, 137 mM NaCl, and 2.7 mM KCl, pH 1.8) was added to 50 μl of the labelling reaction to quench the reaction. 50 μl of the quenched sample was injected onto an immobilized pepsin columns (Enzymate BEH, Waters) (20°C). A VanGuard Pre-column [Acquity UPLC BEH C18 (1.7 μm, 2.1 mm × 5 mm, Waters)] was used to trap the resultant peptides for 3 min. A C18 column (75 μm × 150 mm, Waters, UK) was used to separate the peptides, employing a gradient elution of 0%–40% (v/v) acetonitrile [0.1% (v/v) formic acid] in H_2O (0.3% v/v formic acid) over 7 min at 40 μl min^{-1}. The eluate from the column was infused into a Synapt G2Si mass spectrometer (Waters) that was operated in HDMSE mode. The peptides were separated by ion mobility prior

to CID fragmentation in the transfer cell, to enable peptide identification. Deuterium uptake was quantified at the peptide level. Data analysis was performed using PLGS (v3.0.2) and DynamX (v3.0.0) (Waters). Search parameters in PLGS were: peptide and fragment tolerances = automatic, min fragment ion matches = 1, digest reagent = non-specific, false discovery rate = 4. Restrictions for peptides in DynamX were: minimum intensity = 1000, minimum products per amino acid = 0.3, max. sequence length = 25, max. ppm error = 5, file threshold = 3. Peptides with statistically significant increases/decreases in deuterium uptake were identified using the software Deuteros 2.0. Deuteros was also used to prepare Woods plots. The raw HDX-MS data have been deposited to the ProteomeXchange Consortium via the PRIDE/partner repository with the dataset identifier PXD054754. A summary of the HDX-MS data, as per recommended guidelines, is shown in Supplementary Table S3.

Electrophoretic mobility shift assays

Sense and antisense DNA oligonucleotides were synthesized (by Integrated DNA Technologies, Inc.) which contain the A-box and flanking regions (6 nt at 5′ and 5 nt at 3′) of a human methionine tRNA encoding gene (Human Genome Nomenclature Committee ID: HGNC:34 764). The oligos were modified to have a 6-FAM group covalently attached to the 5′ end of the nucleotide. The final sequences were as follows: (+) 6-FAM-GCCTCGTTAGCGCAGTAGGTAGCGCGTCAG; (−) 6-FAM-CTGACGCGCTACCTACTGCGCTAACGAGGC. These were dissolved to a concentration of 100 μM in Molecular Biology grade water (Invitrogen) and diluted to 4 μM with annealing buffer (10 mM Tris pH 7.5, 50 mM NaCl, and 1 mM EDTA). 25 μl of each oligo were mixed. This mixture was heated to 95°C using a heat block. The block was then allowed to cool slowly back to room temperature then 4°C. The annealed oligos were diluted to a working (4× final) concentration of 40 nM using annealing buffer and were stored at −20°C prior to use. Untagged TFIIIIC5 DBD ΔΔ (pGEX-6P-1 expressed) was diluted approximately 1/20 in 2× binding buffer (40 mM Tris pH 7.5, 100 mM KCl, 2 mM DTT, 10% glycerol, and 20 μg/ml BSA, bovine serum albumin) to a concentration of 8 μM. This was used as the top end of a 2-fold dilution series into 2× binding buffer from 8 μM down to 500 nM. This series was 4× the final concentrations of TFIIIIC5 DBD ΔΔ in the assay. For the 0 nM TFIIIIC5 DBD ΔΔ sample 2× binding buffer was used instead of protein. 5 μl of TFIIIC5 DBD ΔΔ and 10 μl of 2× binding buffer were mixed and allowed to stand on ice for 30 min prior to the addition of 5 μl of the annealed oligos. This was incubated on ice for 60 min prior to loading 10 μl of the mix on a 6% native PAGE DNA retardation gel (Thermo Fisher Scientific). The gel was run for 100 min at 100 V in 0.5× Tris-borate-EDTA buffer. The gel was visualized an iBright imaging system (Thermo Fisher Scientific). Band intensity was quantified using the iBright analysis software. Disappearance of the free probe band was used to determine the percentage bound to TFIIIC5 DBD ΔΔ. Data were fitted using a one site total binding model [$Y = B_{max}*X/(K_D + X) + NS*X + Background$] in GraphPad Prism (Version 9). Results are reported as K_D ± 10% confidence intervals. B_{max} was constrained to not exceed 100% of binding.

Thermal response index calibration assays

A DNA hairpin sequence (Cy5-CTTCTGGCATCGAAGCTGCAAGCTTCGATGCCAGAAG) labelled with Cy5 at the 5′ end was purchased from Integrated DNA Technologies, Inc. Oligo annealing and storage was performed as previously described for electrophoretic mobility shift assays (EMSAs). The assay buffer was 25 mM Tris pH 7.4, 137 mM NaCl, 2.7 mM KCl, 0.5 mM TCEP.HCl, and 0.03% Tween-20. A ∼ 1/10 dilution of TFIIIC5 DBD ΔΔ (in 25 mM Tris pH 7.4, 137 mM NaCl, 2.7 mM KCl, and 2 mM β-mercaptoethanol) was performed into assay buffer. Following this, an eleven-step two-fold dilution series was performed, with 15 μl in each well post dilution. N-myc 1–137 was diluted ∼1/2 using N-myc buffer (25 mM HEPES pH 7.2, 150 mM NaCl, 2 mM β-mercaptoethanol) to 200 μM. 7.5 μl of N-myc (or N-myc buffer) was added to each well of the TFIIIC5 DBD ΔΔ dilution. The labelled DNA was diluted using assay buffer down to 100 nM. 5 μl of DNA was pipetted directly into NanoTemper Dianthus 384-well assay plates. 15 μl of the protein mix was then pipetted into each well. The plate was centrifuged at 500 × *g* for 30 s and sealed. The measurements were performed using auto-excitation on a Dianthus NT.23 instrument at 25°C using DI.Control software (v2.1.1) (Nanotemper Technologies). Laser power was typically 2%–3%. TRIC at an interval of 1.5 s was used to determine the F_{NORM}. The experiment was performed at 25°C. Experiments were performed three times. Data were fitted using a one site total binding model [$Y = B_{max}*X/(K_D + X) + NS*X + Background$] in GraphPad Prism (Version 9). Results are reported as K_D ± one standard deviation.

AlphaFold

AlphaFold2 Multimer calculations were performed with ColabFoldv1.5.5:AlphaFold2 using MMseqs2 [41–43]. For the N-myc:TFIIIC5 DBD calculations N-myc 19–38 (LEFDSLQPCFYPDEDDFYFG) and N-myc 75–89 (PSWVTEMLLENELWG) were the peptide sequences used. The TFIIIC5 DBD sequences were ΔΔ and ΔΔ+AP as documented in Supplementary Table S1. Four seed structures were used to calculate 20 final structures. Three re-cycles were used per structure. The highest ranked structure was relaxed using Amber (version Amber20) [44]. Max iterations 200, energy tolerance 2.39 kcal/mol, stiffness 10.0 kcal/(mol·Å^2), and maximum outer iterations 3. For the modelling of τA with N-myc 1–137, as well as for DNA and DNA–protein complexes AlphaFold3 (https://alphafoldserver.com) was used [45]. The number of recycles was set to three. The seed number was chosen automatically. Five structures were generated per job.

Cell culture, cloning, and transfection

The neuroblastoma cell line SH-EP was grown in RPMI 1640 medium (Thermo Fisher Scientific). HEK293TN cells were grown in DMEM (Thermo Fisher Scientific). Medium was supplemented with 10% fetal calf serum (Biochrom) and penicillin–streptomycin (Sigma–Aldrich). All cells were routinely tested for mycoplasma contamination. For overexpression studies double-stranded DNA fragments based on cDNA sequences of N-myc (wt and mutated) were cloned into a pRRL vector containing an SFFV promoter. For transformation of plasmids, XL-1 blue *E. coli* cells were used. The integrity of the DNA was confirmed by Sanger sequencing (LGC

genomics) of the expression plasmids containing the inserts of interest. For lentivirus production, HEK293TN cells were transfected using PEI. Lentivirus expressing plasmids were transfected together with the packaging plasmid psPAX.2 and the envelope plasmid pMD2.G. Virus-containing supernatant was collected 48 and 72 h after transfection. SH-EP cells were infected with lentiviral supernatant in the presence of 4 μg/ml polybrene for 24 h. Cells were selected for 2 days with puromycin (SH-EP: 2 μg/ml).

Immunoprecipitation assays

For co-immunoprecipitations 20 μl per IP of a 1:1 A/G Dynabeads mix (Thermo Fisher Scientific) was washed with 5 mg/ml BSA–PBS and incubated overnight at 4°C with 2.5 μg antibody against N-myc (Santa Cruz, sc-53993) or IgG as control (Sigma–Aldrich, V9131). Harvested SH-EP cells were lysed with HEPES lysis buffer (20 mM HEPES pH 7.9, 150 mM NaCl, 0.2% v/v NP-40, 0.5 mM EDTA, 10% v/v glycerol, and 2 mM $MgCl_2$), briefly sonicated, incubated for 1 h at 4°C, then 2–4 mg of lysate was added to the bead/antibody mix and incubated for 6–8 h at 4°C. 1%–2% of the lysate was kept as input reference. Lysates were eluted in 2× Laemmli, after washing with HEPES lysis buffer, boiled for 5 min at 95°C. Samples were separated by Bis–Tris–PAGE and transferred to PVDF membranes (Millipore). Membranes were blocked for 1 h with BSA in TBS-T and incubated using the indicated antibodies (TFIIIC5, Bethyl Laboratories, A310-242A; N-myc Santa Cruz, sc-53993) overnight at 4°C. Membranes were washed and probed for 1 h at room temperature with HRP-conjugated secondary antibodies. Images were acquired using the Fusion FX7 EDGE imaging system (Vilber).

Results

N-myc TAD binds to the DNA-binding domain of TFIIIC5

Recently, we have shown a direct protein–protein interaction between N-myc 1–137 and the τA sub-complex of TFIIIC. This was achieved firstly by co-purification of the complex to homogeneity, and secondly by reconstituting the complex by purifying τA and N-myc 1–137 separately, mixing them and following complex formation using SEC [36]. This current work aims to extend this by mapping the interaction further using a combination of molecular biology, biophysics and structural biology approaches.

To map the interaction to a domain of τA we decided to take a divide and conquer approach, purifying each of the domains that make up τA individually. To define the domain boundaries within the τA sub-complex we used the EBI AlphaFold protein structure database (https://alphafold.ebi.ac.uk/) and the yeast τA cryo-EM structure [35]. τA is made up of between three or four domains, depending on the structural arrangement of the largest subunit, TFIIIC3 (Fig. 1A and B). The yeast homologue of TFIIIC3 (τ131, *Saccharomyces cerevisiae*) has two TPR domains which pack against each other in the τA cryo-EM structure. The AlphaFold predictions for human TFIIIC3 suggest that TPR1 (143–571) and TPR2 (620–886) pack tightly together creating a single long TPR domain. TFIIIC5 comprises two domains. Its N-terminus (1–130) forms a β-barrel heterodimerization domain with TFIIIC6 (1–213). The C-terminus of TFIIIC5 (212–519) forms a DBD. These domains were produced through recombinant expression in *E. coli*, but we could not purify any protein for TFIIIC3 TPR2. The three successfully purified domains were used as bait in a pull-down with purified N-myc (1–137), and only the TFIIIC5 DBD was observed to interact (Fig. 1C).

Protein engineering for yield optimization

To generate soluble protein, we engineered the human TFIIIC5 DBD ΔΔ to resemble the equivalent domain in *Schizosaccharomyces pombe*, which yielded a crystal structure, by deleting a long internal loop (Δ345–366) and 49 C-terminal residues (Δ471–519) (Fig. 1D). These C-terminal residues contain a long low complexity acidic region followed by an acidic helix, known as the acidic plug, which packs back into the DNA-binding interface of TFIIIC5 DBD [34, 35]. AlphaFold modelling predicted that engineered and WT proteins have identical folds (Fig. 1D). Pull-downs confirmed the engineered protein interacts with N-myc 1–137, apparently with greater efficiency (Fig. 1E).

N-myc uses two linear peptide sequences to bind TFIIIC5 DBD ΔΔ

To map the N-myc sequence (or sequences) involved in binding, we used NMR ^{1}H-^{15}N HSQC experiments to monitor spectral changes upon titration of unlabelled TFIIIC5 DBD ΔΔ into ^{15}N labelled N-myc proteins. Using the approach we have previously used to map the interaction of the N-myc transactivation domain with Aurora-A kinase, we divided the transactivation domain into two constructs [38]. This increases the signal to noise ratio and reduces the peak overlap within the spectra.

These constructs were firstly, an N-myc 18–72 sequence with an N-terminal GB1 tag, and secondly, a tagless C-terminal N-myc 64–137 sequence. Titration of TFIIIC5 DBD ΔΔ into both proteins was characterized by residue specific peak intensity changes rather than peak shifts. This is likely due to a combination of two factors. Firstly, the slow tumbling of the bound species which results in peak broadening due to an increase in transverse relaxation. Secondly exchange of the bound and unbound species on an intermediate timescale, which also results in peak broadening. Many of these intensity changes were observed early in the titration, with specific peak disappearances observable after addition of 0.1 to 0.3 mole equivalents of TFIIIC5 DBD, consistent with an interaction in intermediate exchange or formation of a 'fuzzy' complex (Fig. 2A and B). To quantify these changes, we calculated peak intensity ratios for spectra with 0.1 mole equivalents of TFIIIC5 DBD ΔΔ with respect to the reference spectra. The intensity ratios of GB1 peaks in the 0.1 mole equivalent ^{1}H–^{15}N HSQC were constant and typically 0.45–0.6, suggesting a uniform decrease in NMR signal intensity upon addition of TFIIIC5 DBD ΔΔ (Fig. 2C). However, some N-myc resonances had ratios which were much lower than this uniform decrease. Residues 27–39, 78–82, and 88–89 had values under 0.2 and residues 22–23, 49–52, 85–86, 90, and 92 had values between 0.2 and 0.3. Residues 65–72, present in both N-myc proteins, and 128–137 were the least affected by addition of TFIIIC5 DBD with intensity ratios higher than for GB1. A similar pattern has been observed previously for Aurora-A kinase, and it could be that binding of a domain to the N-myc sequence alters the dynamics of neighbouring IDR sequences through prevention of any transient self-association [38]. Similar

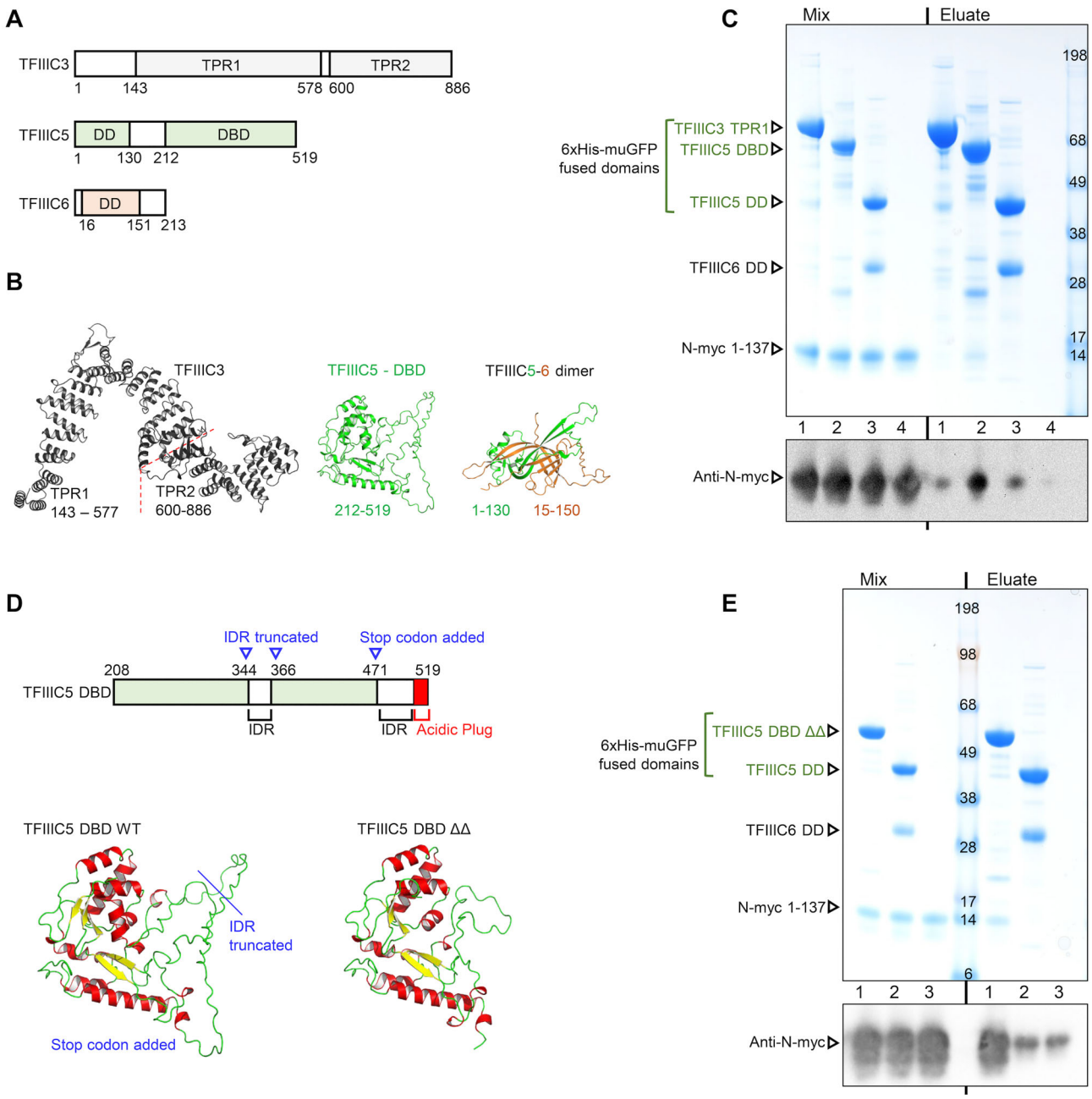

Figure 1. N-myc 1–137 interacts with the DBD of TFIIIC5. (**A**) Domain structures of the proteins that make up the τA sub-complex of TFIIIC. Domain structure is based on the yeast τA structure, and the predicted structures deposited in the EBI AlphaFold repository (https://alphafold.ebi.ac.uk/) for the following UniProt entries TFIIIC3 (Q9Y5Q9); TFIIIC5 (Q9Y5Q8); TFIIIC6 (Q969F1). DD, dimerization domain. (**B**) AlphaFold2 models of TFIIIC3, TFIIIC5 DBD, and TFIIIC5-6 DD, from the EBI AlphaFold repository. (**C**) Coomassie stained SDS–PAGE gel and western blot following PDAs using His-select Cobalt gel. 6xHis-monomeric ultra-stable GFP (muGFP) tagged TFIIIC domains were used as bait. Untagged N-myc 1–137 was prey. (**D**) Top: Schematic of the TFIIIC5 DBD. Alterations made for the DBD ΔΔ expression construct are shown in blue. Bottom: AlphaFold predicted structures of TFIIIC5 DBD proteins. Left, predicted structure of the TFIIIC5 DBD deposited in the EBI AlphaFold repository (https://alphafold.ebi.ac.uk/). Right, AlphaFold3 predicted structure of DBD ΔΔ. Backbone RMSD of the common residues in both models is 0.21 Å. (**E**) Coomassie stained SDS–PAGE gel and western blot following PDAs using His-select Cobalt gel. 6xHis-monomeric ultra-stable GFP (muGFP) tagged TFIIIC domains were bait; untagged N-myc 1–137 prey. Both sets of pull-downs are representative of three independent experiments.

effects were observed when BIN1 was titrated into c-myc 1–88 [46]. A possible contributing factor to the peak disappearances is the slow tumbling of the bound state. This can lead to signal loss through increased transverse relaxation rates. To try to overcome this we used transverse relaxation optimized spectroscopy (TROSY) ^{1}H–^{15}N HSQC experiments. TFIIIC5 DBD ΔΔ was titrated into GB1-N-myc 18–59 as per previous. The pattern of peak disappearance was nearly identical to that observed for 18–72 (Supplementary Fig. S1). While some small corroborating chemical shift perturbations were observed at low mole equivalents, the TROSY did not facilitate characterization of the bound state.

As an orthogonal approach to map the interaction, biotinylated 25-mer residue peptides covering N-myc 1–141 (1–25,

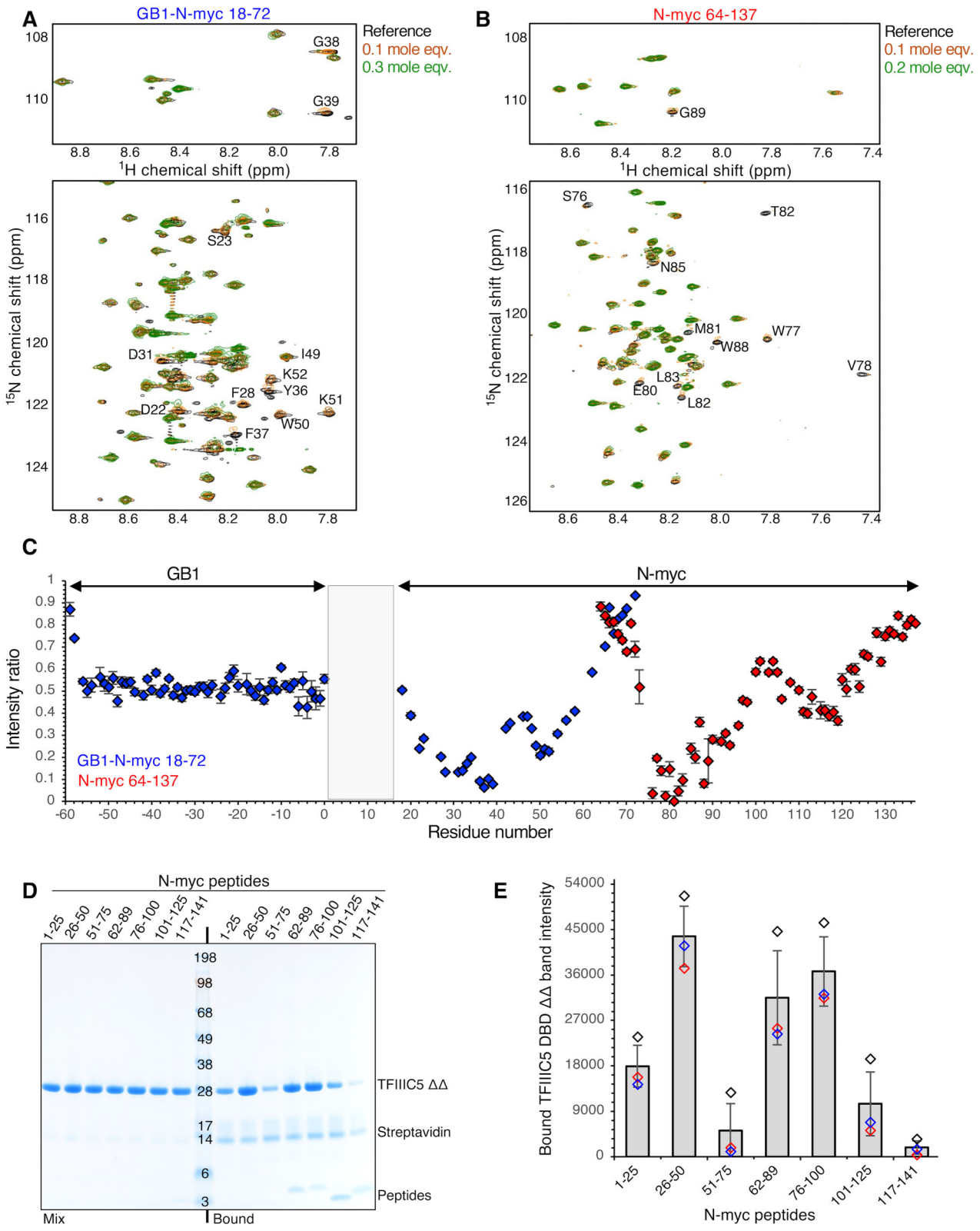

Figure 2. N-myc interacts with the DBD of TFIIIC5 using two peptide sequences. (**A**) ^{1}H–^{15}N HSQC spectra following the titration of TFIIIC5 DBD ΔΔ (208–470; Δ345–366, UniProt: Q9Y5Q8) into ^{15}N-labelled GB1-N-myc 18–72 C27S (UniProt: P04198). Regions of the spectra show the bulk of the backbone resonances (bottom) and the glycine backbone resonances (top). Peaks identified as decreasing in intensity by visual inspection are labelled. Assignments were determined from biological magnetic resonance bank (BMRB) entries 52 047 and 52066. (**B**) As per A, but with ^{15}N-labelled N-myc 64–137. Assignment was taken from BMRB entry 52067. (**C**) Plot of relative peak intensities against residue number. ^{1}H–^{15}N peak intensities for N-myc proteins with 0.1 mole equivalents of ΔΔ divided by the peak intensities of the same peaks in the reference spectra. The GB1 N-terminal tag sequence was plotted with dummy residue numbers -59 for the N-terminus to 0 for C-terminus. (**D**) Coomassie stained SDS–PAGE gel following PDAs using NeutrAvidin resin. Biotinylated N-myc peptides were used as bait. The N-myc peptide numbers are shown above each lane. Untagged TFIIIC5 DBD ΔΔ was used as prey. (**E**) TFIIIC5 DBD ΔΔ eluate bands were quantified using ImageJ for all three repeats of this experiment. Intensity data are plotted along with a bar chart of average intensities ± one standard deviation.

26–50, 51–75, 76–100, 101–125, 117–141) were used as bait and untagged TFIIIC5 DBD ΔΔ as prey in PDAs. An additional N-myc peptide (62–89) was included because it has been observed bound to Aurora-A kinase by X-ray crystallography [47]. The results were broadly in line with the NMR titration. Whereas peptides 51–75 and 117–141 showed minimal binding to TFIIIC5 DBD ΔΔ, and 1–25 showed modest binding, N-myc 26–50, 62–89, and 76–100 showed the clearest binding (Fig. 2D and E).

Hydrogen–deuterium exchange mass spectrometry suggests two binding hotspots on TFIIIC5

To map the binding interface from both the N-myc and TFIIIC5 DBD perspective we used HDX mass spectrometry. 26 N-myc peptides were observed in both experimental conditions (with and without binding partner) covering a total of 94.3% of the sequence. 53 TFIIIC5 DBD ΔΔ shared peptides were observed with 86.6% sequence coverage. Five N-myc peptides covering five different sequences were significantly protected from deuterium exchange upon addition of TFIIIC5 DBD ΔΔ, corresponding to the N-terminal ∼50 residues and a peptide from residue 70–80 (Fig. 3A). This is in reasonable agreement with the mapping experiments using peptides and NMR. Interestingly, three peptides covering ∼20 C-terminal residues of N-myc 1–137 were significantly deprotected in two out of the three time points sampled, which may reflect increased dynamics in a region of the protein that has high helical propensity [38]. This interpretation is consistent with the enhanced NMR peak intensity ratios for this region that were observed upon ΔΔ addition (Fig. 2C).

A total of twelve peptides, covering seven sequences of TFIIIC5 DBD ΔΔ were protected from deuterium exchange upon the addition of N-myc 1–137. These cluster in two regions of the sequence. Five peptides at the N-terminus span four sequences between residues 208 and 267 (Fig. 3A) which sit within the N-terminal winged-helix part of the domain (Fig. 3C). A region closer to the C-terminus of the domain contains a further seven peptides protected upon N-myc binding. This C-terminal region contains two regions (394–407 and 454–466) that have high levels of protection at all time points sampled. Together, the HDX data support a bipartite interaction of N-myc with two patches on the TFIIIC5 DBD surface: one highly protected and likely forming a stable anchor point, and a second that may be more flexible or transient.

N-myc TAD binds to TFIIIC5 DBD ΔΔ with high affinity

Taken together, the NMR titrations, peptide pull-downs, and HDX data suggest that there are two N-myc sequences involved in TFIIIC5 binding; an N-terminal sequence focused around the conserved myc box 0 (N-myc 16–38), and a C-terminal sequence focused around the region of helical propensity involved in Aurora-A interaction (N-myc 74–89), as summarized in Fig. 4A. Next, we measured the binding affinity of the interaction, firstly through FP assays using N-myc peptides 16–38 (MB0) and 61–89 that were chemically synthesized with an N-terminal FAM label. Both peptides bound to TFIIIC5 DBD ΔΔ and the data fitted well to a one-site total binding model using GraphPad Prism. MB0 bound with a dissociation constant of 0.060 μM while 61–89 bound with a dissociation constant of 1.1 μM (Fig. 4B). While this result is consistent with pull-downs shown previously in that both peptides bind TFIIIC5 DBD ΔΔ, it is very clear that MB0 binds much more tightly than 61–89.

With the exception of its constitutive partner MAX, myc binds to other proteins with affinities in the low micromolar range (e.g. GTFIIF 4.9 μM; Bin1 4.2 μM; PNUTS 3.5 μM; TBP-TAF1 5.2 μM; Aurora-A 1 μM) [13, 47–50]. Therefore, the affinity of MB0 for TFIIIC5 DBD ΔΔ was tighter than typical for myc interactions and so we used a second method, isothermal titration calorimetry (ITC), to verify this result. At 37°C, the signature was exothermic, but the protein complex was unstable and precipitated during the titration (data not shown). However, at 10°C the titration resulted in an endothermic heat signature and an equilibrium dissociation constant (K_D) of ∼150 nM, while the stoichiometry was very close to a 1:1 interaction (Supplementary Fig. S2). The observed K_D was ∼2.5-fold lower than the highest K_D observed using FP. However, given the technical differences including the temperatures (10°C for ITC, ∼21°C for FP) these assays are in reasonable agreement. The endothermic heat signature is unusual for protein–protein interactions. This may be due to conformational change in the domain upon binding, consistent with the HDX data; alternatively, it may be due to significant rearrangement of the solvation shell or bound ions forced by protein binding. A recent example of an endothermic heat signature of a protein–protein interaction that was driven by alterations in solvation shell of the protein is the binding of Kap114p to the DNA-binding interface of Yeast TATA-binding protein [51].

To identify residues within N-myc involved in the interaction, we used FP assays with peptides which were modified by truncation or sequence variation. A F28A-Y29A N-myc 16–38 peptide variant bound approximately three-fold less well than observed for the WT peptide (Fig. 5A). A W77A-W88A N-myc 61–89 peptide variant had profoundly negative consequences for binding: we could not determine a K_D, but there was at least a 25-fold reduction in affinity with respect to WT (Fig. 5A). Thus, both binding regions of N-myc have aromatic residues that contribute to the interaction with TFIIIC5. Truncations of the MB0 peptide at its N-terminus had modest effects on affinity compared to the WT peptide. N-myc 20–38 and 24–38 bound with K_D values of approximately 1.5-fold and 3-fold weaker than observed for 16–38, respectively (Fig. 5D). However, N-myc 28–38 had an affinity approximately 14-fold weaker than observed for the 16–38 peptide. Small truncations at the C-terminus also had modest effects on binding. N-myc 16–34 bound 2-fold weaker than 16–38 (Fig. 5C). However, N-myc 16–30 bound approximately 18-fold weaker than the full-length peptide. Taken together these data suggest that the MB0 binding site has an essential core comprising approximately residues 24–34 inclusive (LQPCFYPDEDD). For the N-myc 61–89 peptide, removal of the residues prior (LSPSRGFAEHSSEP) to the Aurora-A interacting helix (AIH, 75–89) observed in the Aurora-A:N-myc crystal structure [47], changed the affinity from ∼1.1 μM to ∼1.6 μM, a minimal effect on binding. Therefore, the interaction of this region is focussed within the AIH (Fig. 5B).

The acidic plug inhibits N-myc binding

Previous structural biology work has shown that the C-terminal helix of TFIIIC5 DBD, known as the acidic plug,

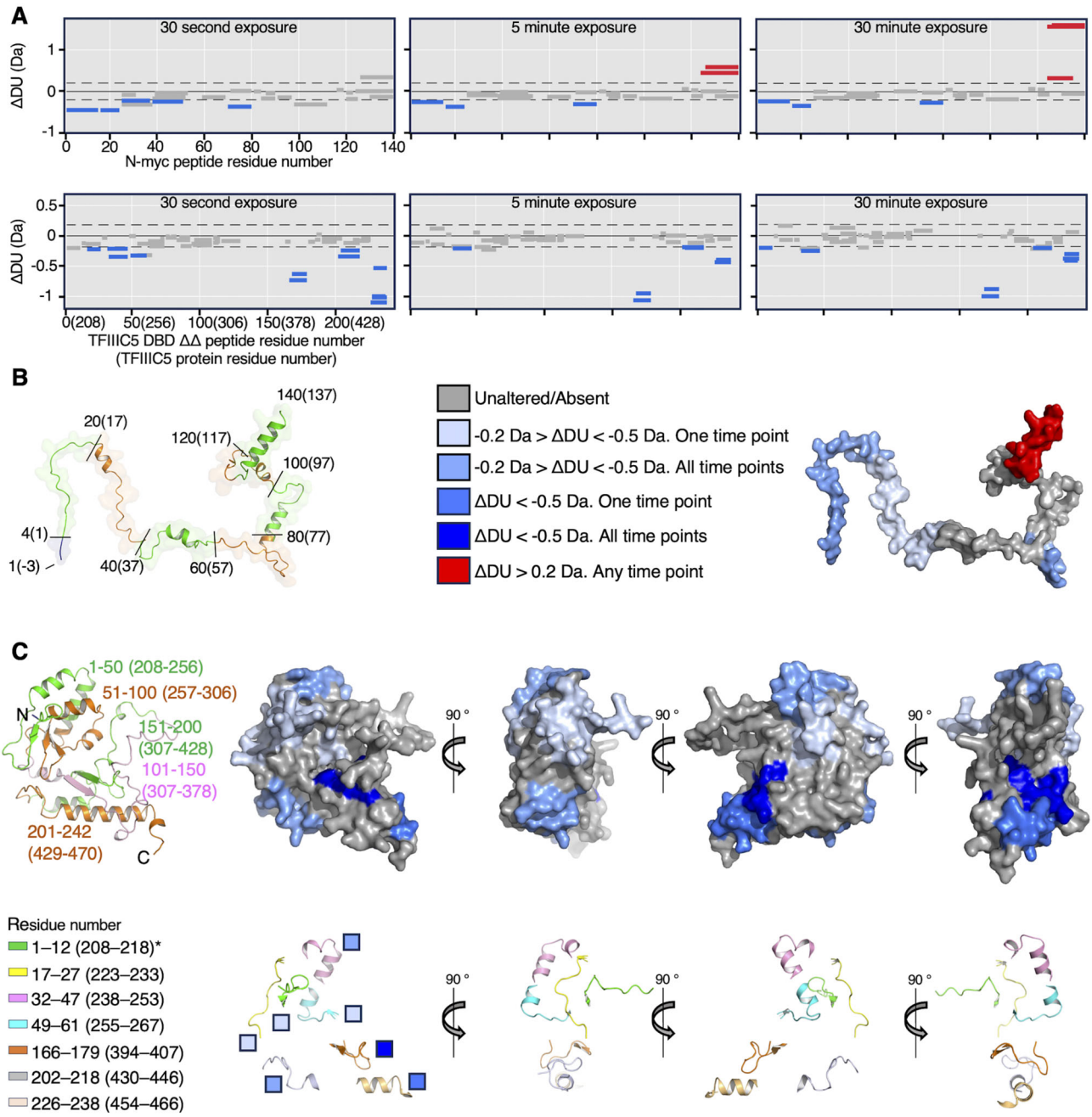

Figure 3. HDX suggests N-myc binds over an extended surface of TFIIIC5 DBD ΔΔ. (**A**) Top: Deuterium uptake difference plots for N-myc 1–137 (UniProt: P04198) in the presence or absence of TFIIIC5 DBD ΔΔ (208–470; Δ345–366, UniProt: Q9Y5Q8). Peptides which had significantly different deuterium incorporation upon addition of TFIIIC5 DBD ΔΔ are labelled in red (increased deuterium incorporation) or blue (reduced deuterium incorporation). Bottom: Deuterium uptake difference plots as above, but for TFIIIC5 DBD ΔΔ in the presence or absence of N-myc 1–137. Numbers in parentheses relate to the native TFIIIC5 protein sequence. (**B**) Left: Cartoon and surface representation of an AlphaFold2 generated model of the N-myc 1–137 construct used in the experiment, including the non-native GAM sequence at the N-terminus. To match the tick marks in the deuterium uptake difference plots for N-myc, every 20 residues of the construct are marked by alternative green and orange colouring and labelled by residue. Numbers in parenthesis are relative to the native N-myc sequence. Right: Surface representation of model shown in the left panel, peptides coloured by the deuterium uptake scale shown. (**C**) Left top: Cartoon representation of an AlphaFold2 generated model of the TFIIIC5 DBD ΔΔ construct used in the experiment, including a non-native G at the N-terminus. To match the tick marks in the deuterium uptake difference plots for TFIIIC5 DBD ΔΔ, every 50 residues of the construct are marked by different colouring. Right top: Surface representation of model shown in the left panel, peptides coloured by the deuterium uptake scale shown in panel (B). Bottom: Cartoon representation of significantly altered TFIIIC5 DBD ΔΔ peptides. The model and views are as shown in panel C above. The level of deuterium uptake is indicated by the colour of the boxes beside the leftmost model; the scale is as per panel (B). The colour key on the left indicates the residue numbering of the altered peptides. Peptides are numbered: as in the HDX data relative to the first amino acid in TFIIIC5 DBD ΔΔ (full-length WT TFIIIC5 protein sequence). ∗ note that the 1–12 peptide includes a residue from the vector, and so the first residue from TFIIIC5 is 208, at position 2 in the peptide.

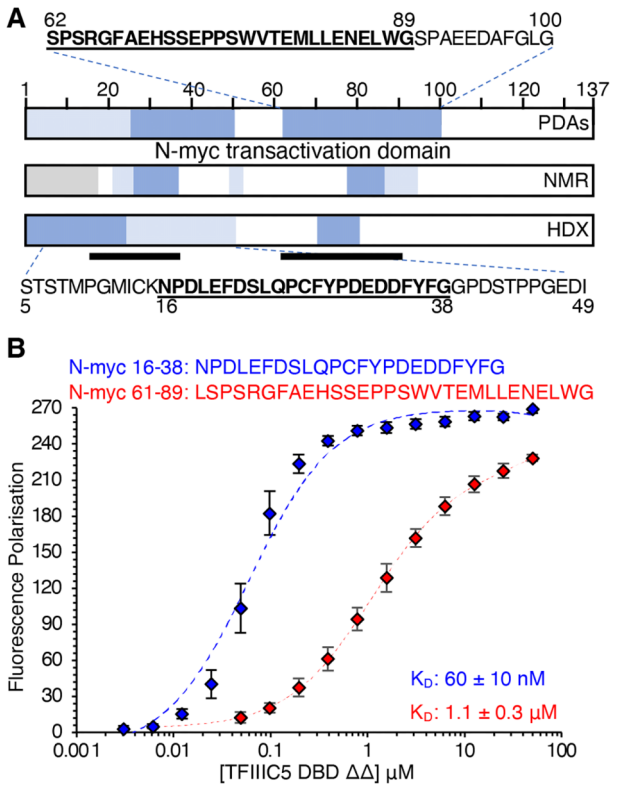

Figure 4. N-myc interacts with the DBD of TFIIIC5 with sub-micromolar affinity. (**A**) Summary of the N-myc peptide mapping experiments described in Figs 2 and 3—PDAs, NMR titrations and HDX mass spectrometry. Tight binding regions are shown in dark blue, intermediate binding regions are shown in light blue. Regions not in the experiment are shown in grey. Underlined protein sequences are known to be important in binding to Aurora-A kinase. The locations of these are also shown by black bars under the HDX schematic. (**B**) 5-FAM labelled N-myc peptides were used as a tracer in FP assays with TFIIIC5 DBD ΔΔ. Error bars are plus and minus one standard deviation of the mean. K_D values were determined using the one site total model in GraphPad Prism. K_D values are given as an average of nine independent experiments plus and minus one standard deviation.

packs back into its DNA-binding surface [34, 35]. However, most of our binding assays have been performed with a construct that lacks this acidic plug, leaving the DNA-binding surface exposed. While we could not produce enough WT full-length DBD for biophysical experiments, we found we could produce enough (~2 mg/l of LB) of a ΔΔ construct, building the acidic plug back into the construct (Fig. 6A). This construct ("ΔΔ+AP") has a low complexity sequence removed (^{487}DEEDEEEEEEEEED^{500}) prior to the acidic plug and contains the loop truncation (Δ345–366) that is in the DBD ΔΔ (Fig. 6A). AlphaFold3 predictions of structure were performed for ΔΔ, ΔΔ+AP, and the WT full-length DBD. In both ΔΔ+AP and WT predictions the C-terminal acidic plug (^{505}DGSENEMETEILDYV^{519}) packs back into the DNA-binding interface in an almost identical conformation. This is a high confidence prediction because the predicted local distance difference test (pLDDT) values are relatively high for the acidic plug (WT full-length pLDDT MAX 82.7, pLDDT mean 63.8; ΔΔ+AP pLDDT MAX 84.0, pLDDT mean 65.8). In addition, the AlphaFold predicted packing of the acidic plug is very similar to the experimentally observed packing in the yeast τA cryo-EM structure (Fig. 6B) [35]. The effect of the addition of the acidic plug to the ΔΔ was to reduce affinity of TFIIIC5 DBD for both MB0 and 61–89 peptides. For MB0 the affinity was reduced approximately 8-fold from 60 to 490 nM, while for the 61–89 peptide the effect was closer to 20-fold from 1.1 to 18.2 μM (Fig. 6C and D). This suggests both binding sites at least partially overlap with the positively charged, acidic plug interacting site of TFIIIC5.

N-myc competes with DNA for TFIIIC5 binding

The positively charged surface of TFIIIC5 that binds the acidic plug is also likely to be the binding site for DNA, with which N-myc would also be expected to compete. To confirm that the human DBD binds DNA, we performed EMSAs using a titration of TFIIIC5 DBD ΔΔ into 5′-FAM labelled double-stranded DNA from the first 30 nucleotides of the tRNA-Met-CAT-1–1 gene, which contains an A-box sequence. The intensity of the free DNA band was reduced, but no discrete new bands were formed. Instead, a smear at the top of the gel suggested non-specific, multiple sites for TFIIIC5 binding on the duplex DNA (Fig. 7A). Indeed, AlphaFold3 modelling of the TFIIIC5 DBD ΔΔ dsDNA interaction suggested that up to four proteins could bind to the duplex DNA used in the experiment (Fig. 7C). The EMSA data are quite variable: quantification of the free DNA and fitting to a one-site binding model gave estimates of the K_D ranging from 127 nM to 446 nM for six independent repeats of the experiment. However, the average value of 293 nM is almost identical to the value of 300 nM K_D reported for the binding of A-box DNA to the crystallization construct of the same domain in *S. pombe*, which also had its acidic plug removed [34]. In addition, the *S. pombe* domain was also found to bind DNA without sequence specificity.

Due to the variability in the EMSA data, we carried out a different assay, thermal response index calibration (TRIC), to determine the effect of N-myc upon TFIIIC5 DBD ΔΔ binding to DNA. A 5′ Cy5 labelled DNA hairpin with a 17 bp double stranded sequence was used as a tracer, based on AlphaFold3 modelling of TFIIIC5 DBD ΔΔ binding to dsDNA (Fig. 7D). This assay generated consistent data between independent repeats, yielding a K_D of 204 ± 7 nM for TFIIIC5 DBD ΔΔ binding to the DNA (Fig. 7E). The addition of 50 μM N-myc 1–137 to all the wells in the titration, representing a 2.5-fold molar excess of N-myc over TFIIIC5 at the top of the titration, had a profound effect on DNA binding (Fig. 7E). The K_D with N-myc was not determined as the curve did not saturate; however, the effect was estimated to be a 10–100-fold decrease in affinity (Fig. 7E). The competition observed is consistent with the predicted binding of N-myc to the DNA-binding surface of TFIIIC5.

Modelling the N-myc:TFIIIC5 interaction

We tried several approaches to obtain a crystal structure of an N-myc peptide with TFIIIC5 DBD ΔΔ but could only produce crystals of the TFIIIC5 DBD ΔΔ alone. The structure was determined to 2.6 Å resolution and is very similar (average backbone RMSD 1.1 Å) to the crystal structure of the equivalent domain in *S. pombe* (Supplementary Fig. S3 and Supplementary Table S4). We modelled N-myc 19–38 and 75–89 peptides with TFIIIC5 DBD ΔΔ and TFIIIC5 DBD FL using AlphaFold2-Multimer (Fig. 8A–F). Twenty models were calculated per complex. The complexes were judged on two

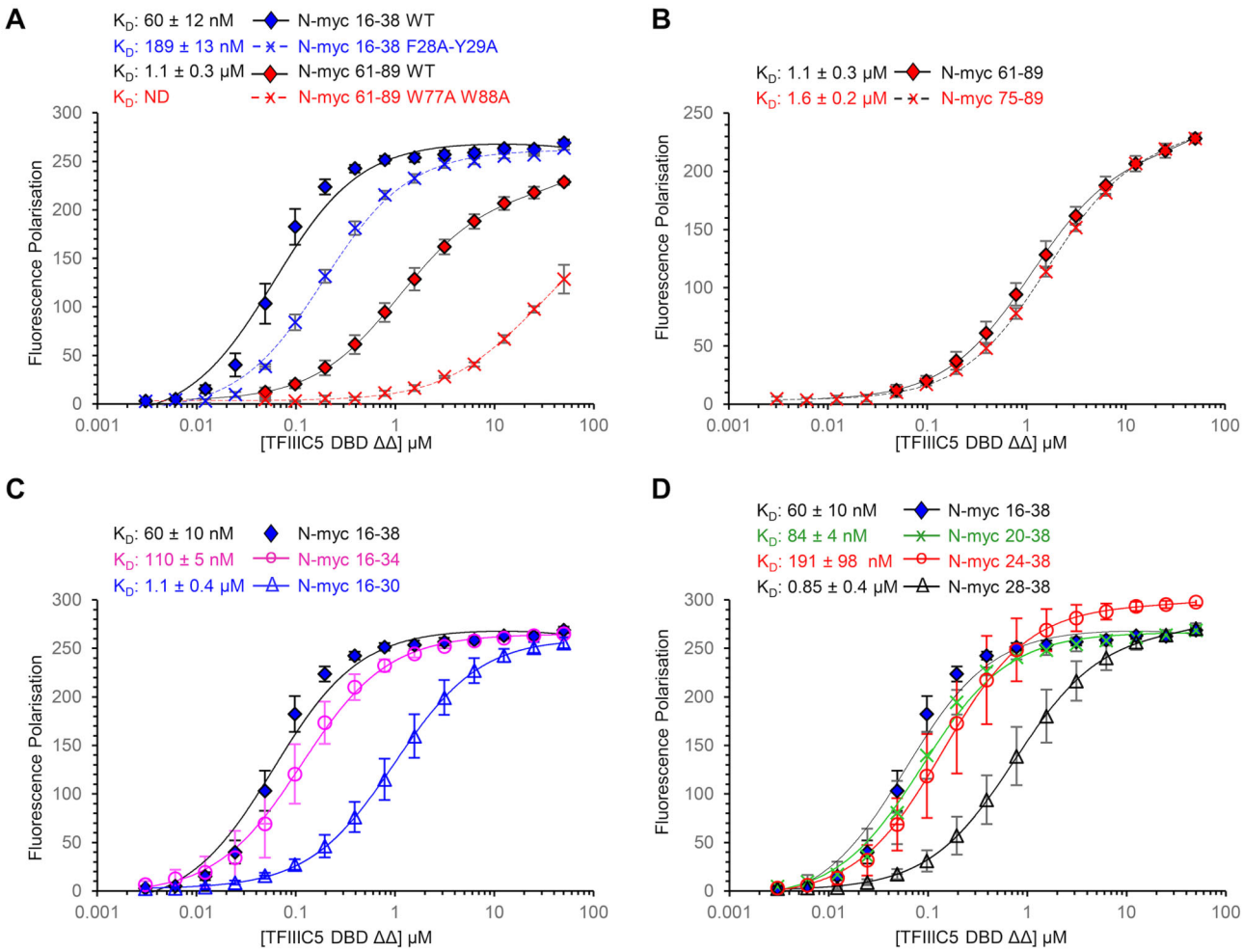

Figure 5. Sequence variation and truncation both reduce the affinity of N-myc peptides for TFIIIC5. 5-FAM labelled N-myc peptides were used as a tracer in FP assays with TFIIIC5 DBD ΔΔ. Mean FP values are plotted ± one standard deviation. Data were fitted using a one-site total binding model in GraphPad Prism. K_D values are the mean ± one standard deviation; ND, not determined. (**A**) WT versus N-myc peptides with sequence substitutions. (**B**) N-myc 61–89 versus N-myc 75–89. (**C**) N-myc 16–38 versus C-terminal truncations. (**D**) N-myc 16–38 versus N-terminal truncations.

criteria: maximum and median interface predicted template modelling (ipTM) scores, and the consistency of the predictions across the models. For N-myc 19–38, analysis of the 20 structural models with the full-length DBD and the ΔΔ variant revealed that the maximum ipTM score was 0.717 and 0.651, respectively (Fig. 8B). N-myc 19–38 was consistently bound to the positively charged surface of TFIIIC5, from which the acidic plug was displaced in the full-length DBD models (Fig. 8C and D). For N-myc 75–89, the maximum ipTM scores from the 20 structural models were 0.737 and 0.516 for the full-length and ΔΔ domains respectively (Fig. 8B). N-myc 75–89 peptide was also predicted to bind to the DNA-binding surface of TFIIIC5. However, there several predicted binding modes at each of the two sites (Fig. 8E and F). As the maximum ipTM score for both 19–38 and 75–89 peptide complexes was >0.7, they both provide plausible models for the interaction. However, the 19–38 peptide is more likely to be correct due to the consistency of the prediction. For the highest ipTM models of the N-myc 19–38:TFIIIC5 interaction, the peptide extends over a large proportion of the DNA-binding surface of TFIIIC5 traversing diagonally across and down the interface. The C-terminus of the motif (^{33}DDFYF^{37}) forms a single helical turn. The hydrophobic ^{37}YF^{38} are packed into a hydrophobic pocket in the winged helix fold at the N-terminus of the domain. This pocket is lined by the side chains of F218, Y290, and W300. The acidic patch of N-myc (^{31}DEDD^{34}) makes several electrostatic contributions to the binding interface, the close interaction of E32 with R266 and K270 likely being the most important. Other notable residues in the interaction include F28 which packs against Y404 of the DBD and F21 which packs into a hydrophobic pocket at the C-terminal helix of the domain. This pocket is lined by the sidechains of R404, L400, I459, and I323.

AlphaFold3 modelling of the τA sub-complex with N-myc 1–137 consistently placed it between the DNA-binding surface of the DBD and the TPR2 domain of TFIIIC3 (Supplementary Fig. S4). However, the binding modes of N-myc were variable, only resembling the mode predicted by AlphaFold2 in one model, with N-myc residues 34–37 occupying near identical positions (Supplementary Fig. S4). The ipTM scores for the N-myc:TFIIIC5 complexes were 0.13–0.14 indicating that these models are unreliable.

Mapping the HDX data on to the models generated by AlphaFold2 suggests a good level of agreement with the N-myc

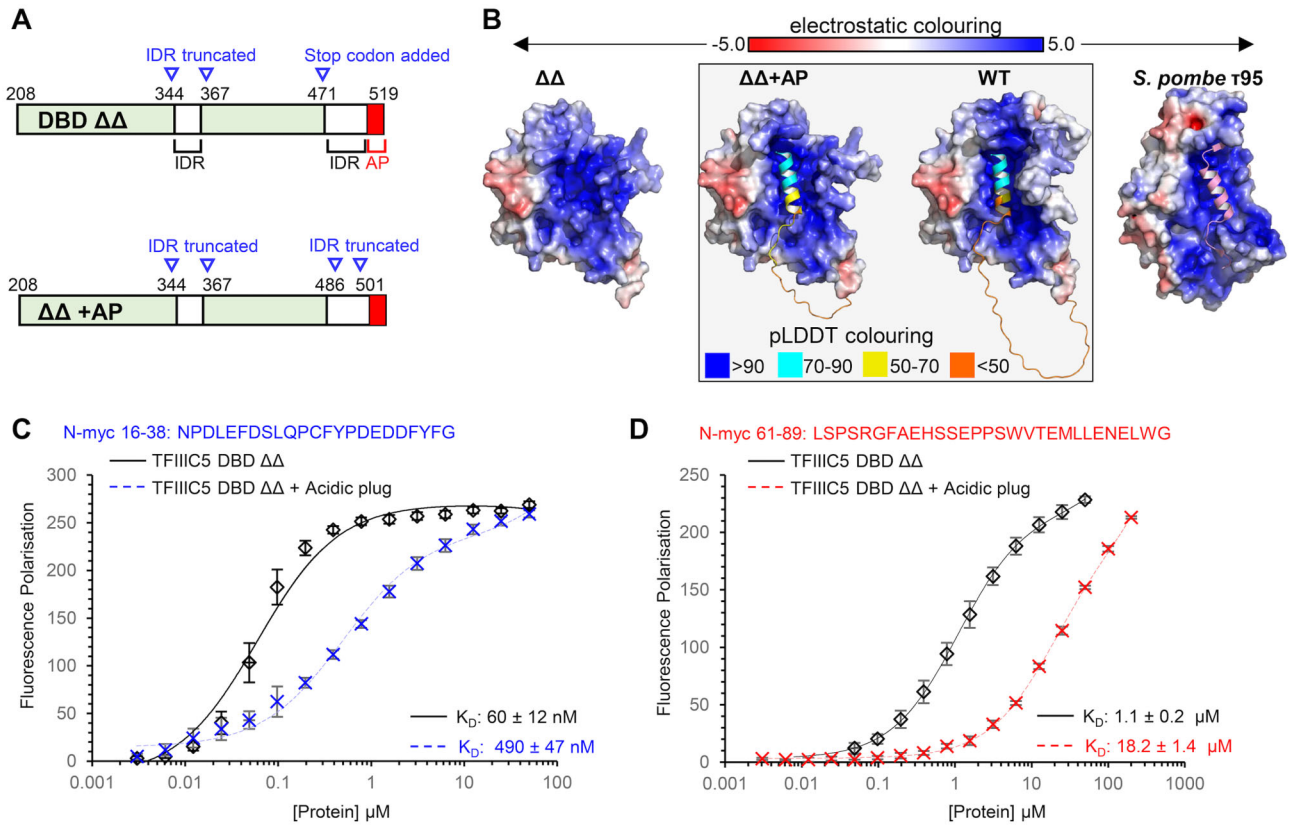

Figure 6. The TFIIIC5 acidic plug reduces the affinity of N-myc peptides for TFIIIC5. (**A**) Schematic of the DBD of TFIIIC5. Alterations made for the DBD ΔΔ (TFIIIC5 208–470; Δ345–366, UniProt: Q9Y5Q8) and DBD ΔΔ +acidic plug (AP) (TFIIIC5 208–519; Δ345–366 Δ487–500) expression constructs are shown in blue. (**B**) AlphaFold3 predicted structures for TFIIIC5 DBD ΔΔ, DBD ΔΔ +AP, and full-length WT TFIIIC5 DBD are shown alongside the cryo-EM structure of the yeast protein τ95, the structure of which was determined in the context of the τA sub-complex [35]. In each case the core domain (211–470 for TFIIIC5 DBD) is shown as a surface representation coloured by electrostatic potential as calculated by APBS. The C-terminal regions of the TFIIIC5 DBD AlphaFold predictions (470–519) are shown as cartoon and coloured by pLDDT score as indicated. The C-terminal region of the yeast τ95, determined by cryo-EM, is also shown as a cartoon but coloured light pink. (**C**) 5-FAM labelled N-myc 16–38 was used as a tracer in FP assays with TFIIIC5 DBD ΔΔ or TFIIIC5 DBD ΔΔ+AP. Error bars are plus and minus one standard deviation of the mean. Data were fitted using a one-site total model in GraphPad Prism. K_D values are given as an average ± one standard deviation. (**D**) Same as (C), except for N-myc 61–89.

19–38 TFIIIC5 model (Supplementary Fig. S5). Four TFIIIC5 peptides which are protected by addition of N-myc (208–218, 223–233, 255–267, and 394–407) are predicted to directly contact N-myc 19–38. The latter two peptides are the ones with the highest levels of protection observed in the HDX experiment. A further two peptides (223–233 and 238–254) are close in space to the predicted N-myc 19–38 binding site. These peptides additionally interact directly with peptides predicted to bind to N-myc 19–38. The only outlier in the HDX data is TFIIIC5 peptide 430–446, which is far from any predicted binding site in the N-myc 19–38 TFIIIC5 model. In contrast, the models of N-myc 75–89 interact with fewer HDX identified peptides. In the model with the highest ipTM score for ΔΔ, N-myc 75–89 contacts three peptides at the winged helix part of the domain, but do not contact the C-terminal 223–233 peptide, which had very high levels of protection in the HDX experiments. By contrast N-myc 75–89 in the WT DBD model with the highest ipTM scores interacts with only the C-terminal peptides and not the winged helix peptides. We therefore conclude that the modelled binding site for N-myc 19–38 to the acidic-plug binding site of TFIIIC5 is more likely to be correct, consistent with it being the higher affinity site that competes with the acidic plug for the pocket on the TFIIIC5 DBD surface.

Mutation in MB0 reduces the TFIIIC5 interaction with N-myc in cells

To validate the molecular basis of the interaction between N-myc and TFIIIC5 in cells, we transfected a neuroblastoma cell line (SH-EP) with either wild type (WT) or variant (F28A-Y29A) HA-tagged full length N-myc. F28A-Y29A N-myc showed a small but statistically robust decrease ($P = 0.0054$) in TFIIIC5 co-immunoprecipitation relative to the WT protein in paired experiments (Fig. 9). This reduction of ∼50% is consistent with our *in vitro* experiments in which the same variant decreased the observed affinity of MB0 for TFIIIC5 ΔΔ ∼3-fold from 60 to 189 nM (Fig. 5A).

Discussion

The myc family of transcription factors are important oncoproteins that regulate genes involved in metabolism, cell proliferation, and other critical processes in cancer cells. The function and regulation of myc proteins involves many protein–protein interactions, but the interplay of these factors and molecular mechanisms that underpin them are poorly understood. Here, we characterize the interaction between N-myc and the DNA-binding surface of TFIIIC5 DBD, an

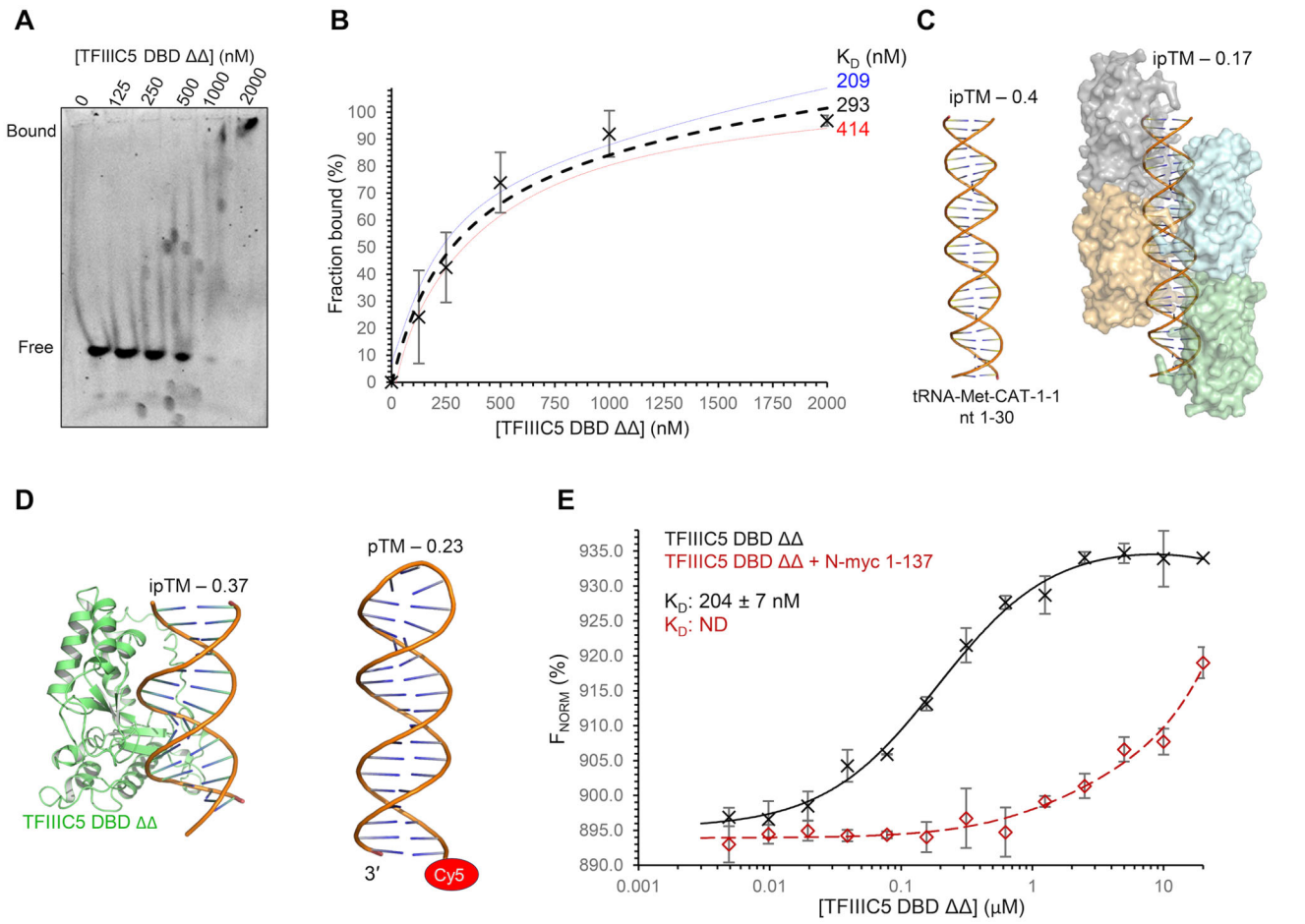

Figure 7. N-myc 1–137 inhibits the binding of TFIIIC5 DNA DBD ΔΔ to double stranded DNA. (**A**) Representative 6% polyacrylamide DNA retardation gel following an EMSA. 5′-6-FAM labelled and annealed dsDNA was used as tracer. Nucleotides 1–30 of the human tRNA-Met-CAT-1–1 gene (GenBank accession number: HG983950.1), including the A-box sequence, was used as the dsDNA. The concentration of TFIIIC5 DBD ΔΔ (TFIIIC5 209–470; Δ 345–466, UniProt: Q9Y5Q8) is indicated above each lane. (**B**) Quantification of the free probe using iBright™ Analysis Software was used to determine the fraction bound. Average values from six independent experiments are shown. Error bars are ± one standard deviation. Data were fitted using a one-site total binding model in GraphPad Prism. The K_D value along with upper and lower bound values at ± 10% confidence intervals. (**C**) AlphaFold3 modelling of the dsDNA (cartoon) used in the EMSA with four TFIIIC DBD ΔΔ bound (surface). The ipTM score is given above the structures. (**D**) Left: AlphaFold3 modelling of A-box DNA bound to ΔΔ. Right: AlphaFold3 modelling of the hairpin DNA sequence used in TRIC assays with ΔΔ. (**E**) TRIC assays using 5′ Cy5 labelled dsDNA hairpin shown modelled in (D). Experiments were performed with (red) or without (black) a constant 50 μM of N-myc 1–137 in each well. Error bars are plus and minus one standard deviation of the mean. K_D values were determined for the titration without N-myc using the one site total model in GraphPad Prism. K_D values are given as an average of three independent experiments ± one standard deviation.

interaction that is thought to contribute to N-myc driven regulation of Pol II transcription and mRNA quality control [14, 36].

The finding that N-myc binds to the DNA-binding surface of the TFIIIC5 DBD was surprising because the TPR domains of TFIIIC3 are established as hubs for other protein–protein interactions. In the cryo-EM structure of yeast TFIIIC (in the context of TFIIIA, TBP, and 5S promoter DNA), the yeast homologue of TFIIIC3, τ131, acts as a central scaffold mediating many of the critical interactions holding the complex together [30]. In addition, τ131 interacts with B double prime 1 (BDP1), a core component of the TFIIIB complex which recruits Pol III [52]. However, the TFIIIC5 DBD:N-myc interaction was observed using a variety of orthogonal approaches and the assignment of this function is therefore robust.

Our findings are consistent with previous data on the competition between TFIIIC and Aurora-A for binding to N-myc [14]. The primary regions of N-myc involved in the Aurora-A interaction are 19–47 and 61–89, which is very similar to the peptides we have shown bind to TFIIIC5 DBD [38, 47]. AlphaFold models predicted that both intrinsically disordered regions of N-myc interact with the same surface of the DBD and the complex might be considered 'fuzzy', consistent with its NMR behaviour. However, while these two regions of N-myc bind Aurora-A with similar affinity (~10 μM), N-myc MB0 has a much higher affinity than N-myc 75–89 for TFIIIC, and so MB0 would dominate the interaction. While MB0 is highly conserved between N-myc and c-myc, both of which interact with TFIIIC, the 75–89 region is poorly conserved. We therefore consider the MB0 interaction to be the most biologically relevant.

The fact that the F28A-Y29A variant has an apparent 3-fold reduction in affinity of N-myc MB0 for TFIIIC5 DBD *in vitro* but also decreases co-immunoprecipitation of full-length N-myc with TFIIIC5 by ~2-fold suggests that our observed MB0 TFIIIC5 interaction is important for the interaction in cells. This is consistent with previously reported BioID proximity labelling experiments using BirA tagged WT c-myc that

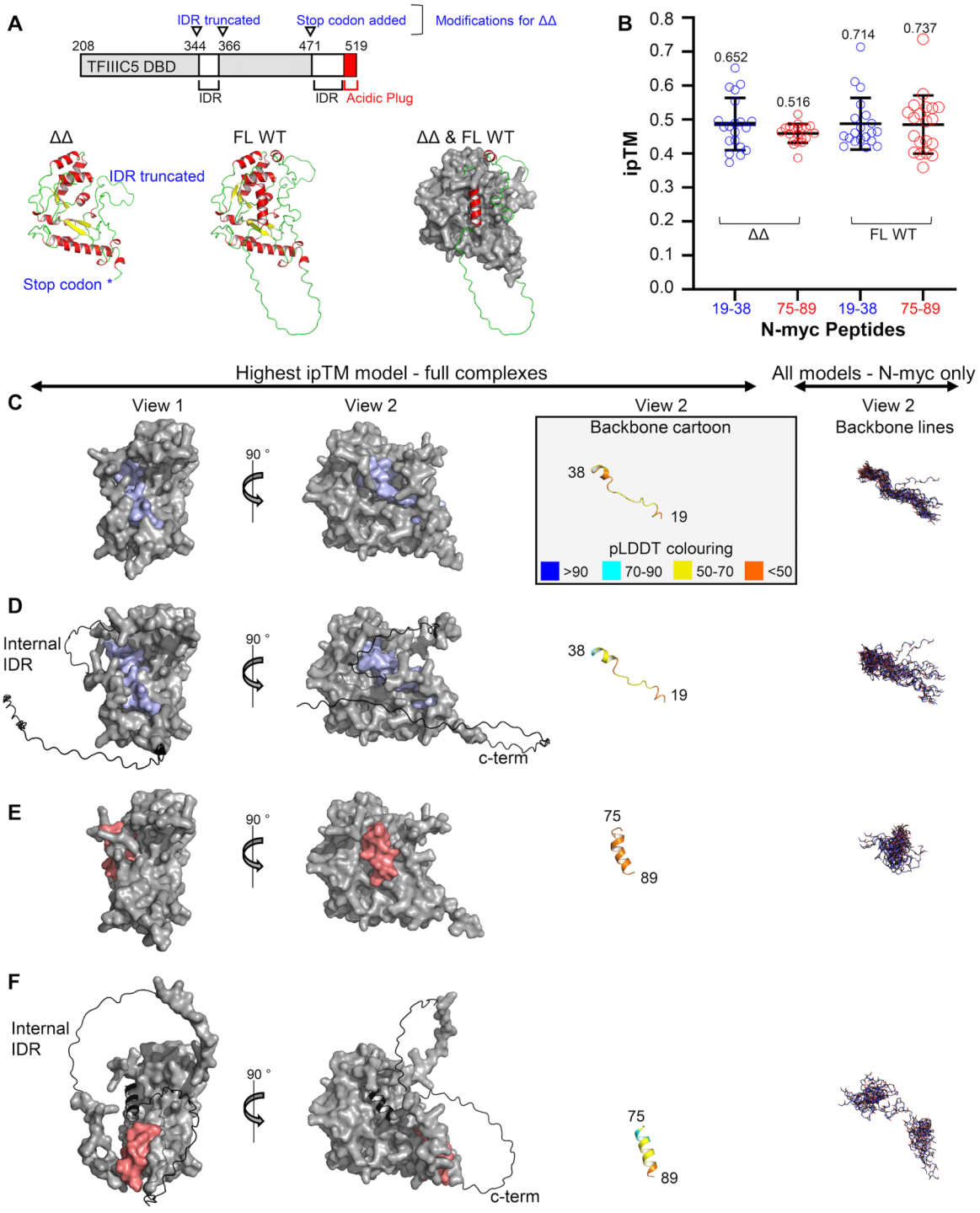

Figure 8. AlphaFold models of the TFIIIC5:N-myc interaction. (**A**) Top: Schematic of the TFIIIC5 DBD (UniProt entry: Q9Y5Q8). Long IDRs are indicated, as is the C-terminal acidic plug which packs back into the DNA-binding interface. Modifications are indicated, in blue, which were introduced into the truncated version of the domain ("ΔΔ"). Bottom left: AlphaFold3 model of TFIIIC5 DBD ΔΔ shown in cartoon representation coloured by secondary structure. Regions modified from WT are indicted in blue beside the model. Bottom middle: AlphaFold3 model of TFIIIC5 DBD full-length wild-type (FL WT). The representation is as per left. Bottom right: Superposed models of FL WT (shown in cartoon representation) with ΔΔ (shown in grey as a surface representation). (**B**) Scatter plot of ipTM scores for all AlphaFold2 multimer models. Twenty models were calculated for each of the four complexes indicated (N-myc 19–38 with ΔΔ, N-myc 75–89 with ΔΔ, N-myc 19–38 with FL WT, and N-myc 75–89 with FL WT). Data are shown as empty circles. The means ± one standard deviation are shown as black bars. The highest value ipTM score for each model is indicated (**C**) AlphaFold2 multimer models of ΔΔ bound to N-myc 19–38. Two views of a surface representation of the highest-ranking complex by ipTM score is shown on the left. ΔΔ is in grey. N-myc 19–38 is in light blue. On the right the N-myc part of the complex is shown without the DBD. Firstly, a cartoon representation of N-myc 19–38 from the complex shown on the left. This is coloured by the pLDDT score (https://github.com/cbalbin-bio/pymol-color-alphafold). On the right is a line representation of the backbone atoms of all the N-myc models. The complexes were aligned in PyMOL using the DBDs. (**D**) As per panel (C), but with FL WT DBD instead of ΔΔ. Regions which are not in the ΔΔ construct are shown in cartoon rather than surface representation. (**E**) As per panel (C), but with N-myc 75–89 (coloured light red) replacing N-myc 19–38. (**F**) As per panel (E), but with FL WT DBD instead of ΔΔ. Regions which are not in the ΔΔ construct are shown in cartoon rather than surface representation.

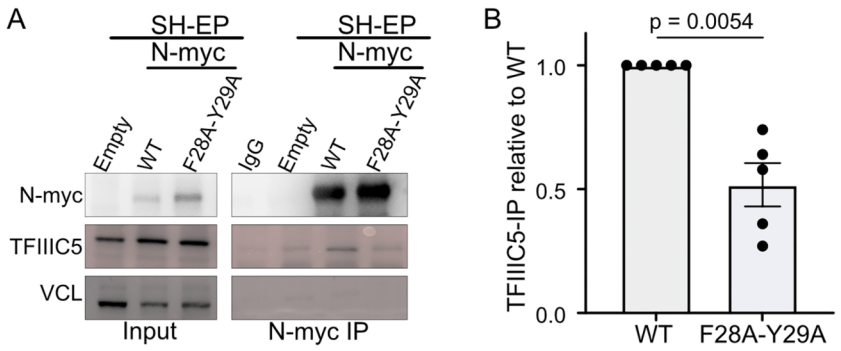

Figure 9. Amino acid substitutions in myc box zero decrease TFIIC5 binding to N-myc in SH-EP cells. (**A**) Western blots from a representative co-immunoprecipitation assay of anti N-myc. The input corresponds to 1% of the amount used for precipitation. Non-specific IgG and VCL were used as controls. (**B**) Co-IPs from five independent experiments were quantified and plotted, showing the mean and standard deviation. The *P*-value was calculated using an unpaired *t*-test with Welch's correction.

resulted in the biotinylation of TFIIIC1, TFIIIC3, TFIIIC4, and TFIIIC5, while deletion of MB0 resulted in the loss of biotinylation of TFIIIC4 and TFIIIC5 [13]. As we took a divide and conquer approach, we cannot rule out the possibility that the interaction is more extensive and may involve other regions of N-myc outside of the transactivation domain or TFIIIC domains which were not part of this study (such as the C-terminal TPR domain of TFIIIC3).

In addition to mapping the interaction on both N-myc and TFIIIC5 DBD, we present AlphaFold models of the interaction. Despite the relatively high ipTM scores (>0.7 for the best models) we would urge caution in their interpretation. We believe that a high-resolution experimental structure of the complexes will be required to accurately describe the molecular basis of these interactions. We are acutely aware of this, because X-ray crystal structures are being published which contradict previously published AlphaFold models [53, 54]. However, we are confident of the location of the MB0 binding site on TFIIIC5 because all the models were similar and displaced the acidic plug, consistent with our experimental data.

It has been postulated that TFIIIC5 DBD is the primary DNA-binding node of τA because it has a large DNA-binding surface, which in part is made up of a well characterized DNA-binding fold, a canonical winged helix [34]. Indeed, the equivalent domain in yeast has been shown to crosslink with DNA in a region close to the A-box sequence [33]. Although structural biology of the holocomplex of TFIIIC in the context of promoter DNA and other transcription factors has begun to emerge, the precise role of the TFIIIC5 DBD is still unknown. In the human TFIIIC–tDNA promoter structure, the density for the domain is absent. This may not be surprising as DNA is not bound to the τA sub-complex in this structure [29]. However, in recent structures of yeast TFIIIC, bound to tDNA and 5S rDNA promoter sequences, density for the T95 (TFIIIC5 homologue) DBD is also absent even though in both structures DNA is bound to τA, predominantly via the C-terminal TPR domain of the TFIIIC3 homologue, τ131 [30, 55]. In the case of the tDNA promoter there is evidence that the DBD may be dynamically binding DNA close to the A-box sequence, but the role of this interaction in TFIIIC function remains to be fully determined [55]. From the evidence thus far, the contacts driving the τA DNA interaction are almost exclusively outside of the DBD of TFIIIC5. However, it should be noted that the observed DNA binding modes of yeast τA was very different for tDNA and rDNA promoters. There may be significant plasticity in how DNA is engaged by τA when different binding partners are present. The other binding partners critical to the function of the N-myc:TFIIIC complex have yet to be fully determined and may play important roles in how τA engages DNA. In this context, ideas on how the N-myc:TFIIIC5 DBD interaction fit into the broader context of Pol II gene expression, or mRNA transcript quality control, must be viewed as speculative. If the DBD is mostly in the DNA bound state, it may be that N-myc acts as a recycling factor, or avidity trap, keeping TFIIIC close to E-box DNA when it is displaced from A- and B-box DNA through the action of polymerases or other kinetic activities involved in transcription. Alternatively if the DBD is mostly available, even in the DNA bound state of TFIIIC, it may be that N-myc is interacting with the already bound complex and influencing the recruitment of other proteins to the locus, such as the cohesin complex or the nuclear exosome complex, complexes which have been shown to be associated factors in the N-myc:TFIIIC complex [14, 36].

MB0 (LEFDSLQPCFYPDEDDFYFG) has an amino acid composition very similar to that defined by Sanborn and colleagues as an acidic 'core activator domain', in that it contains a high proportion of acidic residues interspersed with bulky hydrophobic residues [56]. While this approximate configuration of acidic activator sequences has been known for a long time, only recently have systematic mutagenesis screens shown that both the acidic and hydrophobic components are important for transactivation [57–60]. MB0 has now been shown to interact with two DBDs, its own DBD that is formed with MAX and now TFIIIC5. It has been postulated that the acidic sequences in transactivation domains are primarily for solubilizing the hydrophobic sequences which are the primary binding sequences facilitating transactivation [58, 60]. However, at least in these cases the acidic patches do seem to be important binding determinants. Given that c-myc has already been shown to bind to the DNA-binding interface of TBP, it could be that association with DNA-binding interfaces is a general feature of myc interactions [50]. This may have functions such as facilitation of pre-initiation complex formation as has been proposed for TBP binding [50]. It also could help to capture DNA-binding complexes which are dynamically removed from the DNA through the action of polymerases or complex disassembly. In effect, myc proteins could help prevent diffusion of these complexes away from E-box sequences.

Acknowledgements

We would like to thank our Leeds colleagues: Dr Arnout Kalverda and Dr Bob Schiffrin for assistance in NMR data collection and analysis; Dr Iain Manfield for supporting ITC and Dianthus instruments; Dr Jennifer Miles and Dr Chi Trinh as well as staff scientists on the I04 beamline at Diamond Light Source for assistance with X-ray crystallography data collection; Dr Sri Ranjani Ganji for assistance in HDX mass spectrometry data acquisition and analysis. We would like to thank Prof. Roland Dunbrack (Fox Chase Cancer Centre) for helpful discussions on AlphaFold modelling. Finally, we would like to thank Dr Filippo Prischi (King's College London) and Dr Ravindra Chaudhari (NanoTemper Technologies GmbH) for help setting up the TRIC assays.

Author contributions: Eoin Leen (Conceptualization, Formal analysis, Funding acquisition, Investigation, Methodology, Resources, Validation, Visualization, Writing – original draft, Writing – review and editing), Sharon Yeoh (Conceptualization, Formal analysis, Investigation, Methodology, Validation, Writing – review and editing), Eka Sahak (Formal analysis, Investigation, Methodology), Elizabeth Mitchell (Formal analysis, Investigation), Gemma Wildsmith (Formal analysis, Investigation, Methodology), Matthew Batchelor (Resources, Investigation, Supervision, Writing – review and editing), Antonio N. Calabrese (Supervision, Writing – review and editing), Gabriele Büchel (Conceptualization, Funding acquisition, Supervision, Writing – review and editing), and Richard Bayliss (Conceptualization, Funding acquisition, Supervision, Writing – review and editing)

Supplementary data

Supplementary data is available at NAR online.

Conflict of interest

None declared.

Funding

R.B., E.L., and S.Y. were supported by a Medical Research Council Project Award [grant number MR/V029975/1]. G.B. was supported by grants from the Mildred Scheel Junior Research Center Program. M.B. was supported by the Biotechnology and Biological Sciences Research Council BBSRC [grant number BB/V003577/1 and BB/V003577/2]. A.N.C. was supported by a Sir Henry Dale Fellowship jointly funded by the Wellcome Trust and the Royal Society [Grant Number 220628/Z/20/Z]. Funding from the Biotechnology and Biological Sciences Research Council enabled the purchase of mass spectrometry equipment [grant number BB/M012573/1]. Funding for ITC and NMR instrumentation was provided by the Wellcome Trust [grant numbers 094232/Z/10/Z; 104920/Z/14/Z]. The Dianthus NT.23 instrument was funded by an MRC World Class Labs award [MC_PC_MR/Y002482/1]. Funding to pay the Open Access publication charges for this article was provided by a Jisc Read & Publish agreement between the University of Leeds and Oxford University Press.

Data availability

The mass spectrometry proteomics data have been deposited to the ProteomeXchange Consortium via the PRIDE partner repository with the dataset identifier PXD054754 [61]. The highest ranked and relaxed AlphaFold Multimer models were deposited in the ModelArchive (https://www.modelarchive.org/). The models are available using the following project IDs and DOIs: TFIIIC5 209-529 WT with N-myc 19-38. Project ID: ma-6bh7c. DOI: 10.5452/ma-6bh7c. TFIIIC5 209-519 WT with N-myc 75-89: Project ID: ma-rtr8n. DOI: 10.5452/ma-rtr8n. TFIIIC5 ΔΔ with N-myc 19-38: Project ID: ma-xfvw4. DOI: 10.5452/ma-xfvw4. TFIIIC5 ΔΔ with N-myc 75-89: Project ID: ma-4q6qn. DOI: 10.5452/ma-4q6qn. The coordinates of TFIIIC5 DBD ΔΔ have been deposited in the protein data bank (www.rcsb.org) with the entry identifier 9GI4.

References

1. Nair SK, Burley SK. X-ray structures of Myc-Max and Mad-Max recognizing DNA. *Cell* 2003;112:193–205. https://doi.org/10.1016/S0092-8674(02)01284-9
2. Blackwell TK, Kretzner L, Blackwood EM *et al.* Sequence-specific DNA binding by the c-myc protein. *Science* 1990;250:1149–51. https://doi.org/10.1126/science.2251503
3. Blackwood EM, Lüscher B, Eisenman RN. Myc and Max associate in vivo. *Genes Dev* 1992;6:71–80. https://doi.org/10.1101/gad.6.1.71
4. Jha RK, Kouzine F, Levens D. MYC function and regulation in physiological perspective. *Front Cell Dev Biol* 2023;11:1268275. https://doi.org/10.3389/fcell.2023.1268275
5. Schaub FX, Dhankani V, Berger AC *et al.* Pan-cancer alterations of the MYC oncogene and its proximal network across the cancer genome atlas. *Cell Syst* 2018;6:282–300. https://doi.org/10.1016/j.cels.2018.03.003
6. Nie Z, Hu G, Wei G *et al.* c-myc is a universal amplifier of expressed genes in lymphocytes and embryonic stem cells. *Cell* 2012;151:68–79. https://doi.org/10.1016/j.cell.2012.08.033
7. Lin CY, Lovén J, Rahl PB *et al.* Transcriptional amplification in tumor cells with elevated c-myc. *Cell* 2012;151:56–67. https://doi.org/10.1016/j.cell.2012.08.026
8. Nie Z, Guo C, Das SK *et al.* Dissecting transcriptional amplification by MYC. *eLife* 2020;9:e52483. https://doi.org/10.7554/eLife.52483
9. Gomez-Roman N, Grandori C, Eisenman RN *et al.* Direct activation of RNA polymerase III transcription by c-myc. *Nature* 2003;421:290–4. https://doi.org/10.1038/nature01327
10. Grandori C, Gomez-Roman N, Felton-Edkins ZA *et al.* c-myc binds to human ribosomal DNA and stimulates transcription of rRNA genes by RNA polymerase I. *Nat Cell Biol* 2005;7:311–8. https://doi.org/10.1038/ncb1224
11. Arabi A, Wu S, Ridderstråle K *et al.* c-myc associates with ribosomal DNA and activates RNA polymerase I transcription. *Nat Cell Biol* 2005;7:303–10. https://doi.org/10.1038/ncb1225
12. de Pretis S, Kress TR, Morelli MJ *et al.* Integrative analysis of RNA polymerase II and transcriptional dynamics upon MYC activation. *Genome Res* 2017;27:1658–64. https://doi.org/10.1101/gr.226035.117
13. Kalkat M, Resetca D, Lourenco C *et al.* MYC protein interactome profiling reveals functionally distinct regions that cooperate to drive tumorigenesis. *Mol Cell* 2018;72:836–48. https://doi.org/10.1016/j.molcel.2018.09.031
14. Büchel G, Carstensen A, Mak K-Y *et al.* Association with Aurora-A controls N-MYC-dependent promoter escape and pause release of RNA polymerase II during the cell cycle. *Cell Rep* 2017;21:3483–97.

15. Rahl PB, Lin CY, Seila AC *et al.* c-Myc regulates transcriptional pause release. *Cell* 2010;141:432–45. https://doi.org/10.1016/j.cell.2010.03.030
16. Patange S, Ball DA, Wan Y *et al.* MYC amplifies gene expression through global changes in transcription factor dynamics. *Cell Rep* 2022;38:110292. https://doi.org/10.1016/j.celrep.2021.110292
17. Yang J, Chung C-I, Koach J *et al.* MYC phase separation selectively modulates the transcriptome. *Nat Struct Mol Biol* 2024;31:1567–79. https://doi.org/10.1038/s41594-024-01322-6
18. Rickman DS, Schulte JH, Eilers M. The expanding world of N-MYC–driven tumors. *Cancer Discov* 2018;8:150–63. https://doi.org/10.1158/2159-8290.CD-17-0273
19. Seeger RC, Brodeur GM, Sather H *et al.* Association of multiple copies of the N- myc oncogene with rapid progression of neuroblastomas. *N Engl J Med* 1985;313:1111–6. https://doi.org/10.1056/NEJM198510313131802
20. Brodeur GM, Seeger RC, Schwab M *et al.* Amplification of N- myc in untreated Human neuroblastomas correlates with advanced disease stage. *Science* 1984;224:1121–4. https://doi.org/10.1126/science.6719137
21. Schwab M, Alitalo K, Klempnauer K-H *et al.* Amplified DNA with limited homology to myc cellular oncogene is shared by human neuroblastoma cell lines and a neuroblastoma tumour. *Nature* 1983;305:245–8. https://doi.org/10.1038/305245a0
22. Malynn BA, de Alboran IM, O'Hagan RC *et al.* N-myc can functionally replace c-myc in murine development, cellular growth, and differentiation. *Genes Dev.* 2000;14:1390–9. https://doi.org/10.1101/gad.14.11.1390
23. Kato GJ, Barrett J, Villa-Garcia M *et al.* An amino-terminal c-myc domain required for neoplastic transformation activates transcription. *Mol Cell Biol* 1990;10:5914–20.
24. Wang L, Chen C, Song Z *et al.* EZH2 depletion potentiates MYC degradation inhibiting neuroblastoma and small cell carcinoma tumor formation. *Nat Commun* 2022;13:12. https://doi.org/10.1038/s41467-021-27609-6
25. Heidelberger JB, Voigt A, Borisova ME *et al.* Proteomic profiling of VCP substrates links VCP to K6-linked ubiquitylation and c-myc function. *EMBO Rep* 2018;19:e44754. https://doi.org/10.15252/embr.201744754
26. Koch H, Zhang R, Verdoodt B *et al.* Large-scale identification of c-MYC-associated proteins using a combined TAP/MudPIT approach. *Cell Cycle* 2007;6:205–17. https://doi.org/10.4161/cc.6.2.3742
27. Ewing RM, Chu P, Elisma F *et al.* Large-scale mapping of human protein–protein interactions by mass spectrometry. *Mol Syst Biol* 2007;3:89. https://doi.org/10.1038/msb4100134
28. Schultz P, Marzouki N, Marck C *et al.* The two DNA-binding domains of yeast transcription factor tau as observed by scanning transmission electron microscopy. *EMBO J* 1989;8:3815–24. https://doi.org/10.1002/j.1460-2075.1989.tb08559.x
29. Seifert-Davila W, Girbig M, Hauptmann L *et al.* Structural insights into human TFIIIC promoter recognition. *Sci Adv* 2023;9:eadh2019. https://doi.org/10.1126/sciadv.adh2019
30. Talyzina A, Han Y, Banerjee C *et al.* Structural basis of TFIIIC-dependent RNA polymerase III transcription initiation. *Mol Cell* 2023;83:2641–52. https://doi.org/10.1016/j.molcel.2023.06.015e7.
31. Moir RD, Sethy-Coraci I, Puglia K *et al.* A tetratricopeptide repeat mutation in yeast transcription factor IIIC $_{131}$ (TFIIIC $_{131}$) facilitates recruitment of tfiib-related factor TFIIIB $_{70}$. *Mol Cell Biol* 1997;17:7119–25. https://doi.org/10.1128/MCB.17.12.7119
32. Liao Y, Willis IM, Moir RD. The Brf1 and Bdp1 subunits of transcription factor TFIIIB bind to overlapping sites in the tetratricopeptide repeats of Tfc4. *J Biol Chem* 2003;278:44467–74. https://doi.org/10.1074/jbc.M308354200
33. Braun BR, Bartholomew B, Kassavetis GA *et al.* Topography of transcription factor complexes on the *Saccharomyces cerevisiae 5* S RNA gene. *J Mol Biol* 1992;228:1063–77. https://doi.org/10.1016/0022-2836(92)90315-B
34. Taylor NMI, Baudin F, von Scheven G *et al.* RNA polymerase III-specific general transcription factor IIIC contains a heterodimer resembling TFIIF Rap30/Rap74. *Nucleic Acids Res* 2013;41:9183–96. https://doi.org/10.1093/nar/gkt664
35. Vorländer MK, Jungblut A, Karius K *et al.* Structure of the TFIIIC subcomplex τa provides insights into RNA polymerase III pre-initiation complex formation. *Nat Commun* 2020;11:4905. https://doi.org/10.1038/s41467-020-18707-y
36. Vidal R, Leen E, Herold S *et al.* Association with TFIIIC limits MYCN localization in hubs of active promoters and chromatin accumulation of non-phosphorylated RNA Polymerase II. *eLife* 2024; 13:RP94407. https://doi.org/10.7554/eLife.94407
37. Bagnéris C, Ageichik AV, Cronin N *et al.* Crystal structure of a vFlip-ikkγ complex: insights into viral activation of the IKK signalosome. *Mol Cell* 2008;30:620–31. https://doi.org/10.1016/j.molcel.2008.04.029
38. Rejnowicz E, Batchelor M, Leen E *et al.* Exploring the dynamics and interactions of the N-myc transactivation domain through solution Nuclear Magnetic resonance spectroscopy. *Biochem J* 2024;481:1535–56, https://doi.org/10.1042/BCJ20240248
39. Delaglio F, Grzesiek S, Vuister GW *et al.* NMRPipe: a multidimensional spectral processing system based on UNIX pipes. *J Biomol NMR* 1995;6:277–93. https://doi.org/10.1007/BF00197809
40. Vranken WF, Boucher W, Stevens TJ *et al.* The CCPN data model for NMR spectroscopy: development of a software pipeline. *Proteins* 2005;59:687–96. https://doi.org/10.1002/prot.20449
41. Mirdita M, Schütze K, Moriwaki Y *et al.* ColabFold: making protein folding accessible to all. *Nat Methods* 2022;19:679–82. https://doi.org/10.1038/s41592-022-01488-1
42. Jumper J, Evans R, Pritzel A *et al.* Highly accurate protein structure prediction with AlphaFold. *Nature* 2021;596:583–9. https://doi.org/10.1038/s41586-021-03819-2
43. Evans R, O'Neill M, Pritzel A *et al.* Protein complex prediction with AlphaFold-multimer. *bioRxiv*, https://doi.org/10.1101/2021.10.04.463034, 04 October 2021, preprint; not peer reviewed.
44. Case DA, Cheatham TE, Darden T *et al.* The Amber biomolecular simulation programs. *J Comput Chem* 2005;26:1668–88. https://doi.org/10.1002/jcc.20290
45. Abramson J, Adler J, Dunger J *et al.* Accurate structure prediction of biomolecular interactions with AlphaFold 3. *Nature* 2024;630:493–500. https://doi.org/10.1038/s41586-024-07487-w
46. Andresen C, Helander S, Lemak A *et al.* Transient structure and dynamics in the disordered c-myc transactivation domain affect Bin1 binding. *Nucleic Acids Res* 2012;40:6353–66. https://doi.org/10.1093/nar/gks263
47. Richards MW, Burgess SG, Poon E *et al.* Structural basis of N-Myc binding by Aurora-A and its destabilization by kinase inhibitors. *Proc. Natl. Acad. Sci. USA* 2016;113:13726–31. https://doi.org/10.1073/pnas.1610626113
48. Pineda-Lucena A, Ho CSW, Mao DYL *et al.* A structure-based model of the c-myc/Bin1 protein interaction shows alternative splicing of Bin1 and c-myc phosphorylation are key binding determinants. *J Mol Biol* 2005;351:182–94. https://doi.org/10.1016/j.jmb.2005.05.046
49. Wei Y, Redel C, Ahlner A *et al.* The MYC oncoprotein directly interacts with its chromatin cofactor PNUTS to recruit PP1 phosphatase. *Nucleic Acids Res* 2022;50:3505–22. https://doi.org/10.1093/nar/gkac138
50. Wei Y, Resetca D, Li Z *et al.* Multiple direct interactions of TBP with the MYC oncoprotein. *Nat Struct Mol Biol* 2019;26:1035–43. https://doi.org/10.1038/s41594-019-0321-z
51. Liao C-C, Wang Y-S, Pi W-C *et al.* Structural convergence endows nuclear transport receptor Kap114p with a transcriptional repressor function toward TATA-binding protein. *Nat Commun* 2023;14:5518. https://doi.org/10.1038/s41467-023-41206-9

52. Male G, von Appen A, Glatt S *et al.* Architecture of TFIIIC and its role in RNA polymerase III pre-initiation complex assembly. *Nat Commun* 2015;6:7387. https://doi.org/10.1038/ncomms8387
53. Forker K, Fleming MC, Pearce KH *et al.* Crystal structure of MAGEA4 MHD-RAD18 R6BD reveals a flipped binding mode compared to AlphaFold2 prediction. *EMBO J* 2024;43:2835–9. https://doi.org/10.1038/s44318-024-00140-2
54. Griffith-Jones S, Álvarez L, Mukhopadhyay U *et al.* Response to Forker et-al. *EMBO J* 2024;43:2840–2. https://doi.org/10.1038/s44318-024-00141-1
55. Seifert-Dávila W, Chaban A, Baudin F *et al.* Structural and kinetic insights into tRNA promoter engagement by yeast general transcription factor TFIIIC. *Nucleic Acids Res* 2025; 53:gkae1174. https://doi.org/10.1093/nar/gkae1174
56. Sanborn AL, Yeh BT, Feigerle JT *et al.* Simple biochemical features underlie transcriptional activation domain diversity and dynamic, fuzzy binding to Mediator. *eLife* 2021;10:e68068. https://doi.org/10.7554/eLife.68068
57. Sigler PB. Acid blobs and negative noodles. *Nature* 1988;333:210–2. https://doi.org/10.1038/333210a0
58. Staller MV, Holehouse AS, Swain-Lenz D *et al.* A high-throughput mutational scan of an intrinsically disordered acidic transcriptional activation domain. *Cell Syst* 2018;6:444–55. https://doi.org/10.1016/j.cels.2018.01.015
59. DelRosso N, Tycko J, Suzuki P *et al.* Large-scale mapping and mutagenesis of human transcriptional effector domains. *Nature* 2023;616:365–72. https://doi.org/10.1038/s41586-023-05906-y
60. Staller MV, Ramirez E, Kotha SR *et al.* Directed mutational scanning reveals a balance between acidic and hydrophobic residues in strong human activation domains. *Cell Syst* 2022;13:334–45. https://doi.org/10.1016/j.cels.2022.01.002
61. Perez-Riverol Y, Bai J, Bandla C *et al.* The PRIDE database resources in 2022: a hub for mass spectrometry-based proteomics evidences. *Nucleic Acids Res* 2022;50:D543–52. https://doi.org/10.1093/nar/gkab1038

Received: October 22, 2024. **Revised:** February 7, 2026. **Accepted:** February 11, 2026